Mon. Not. R. Astron. Soc. **000**, 000–000 (1997)

Dust shells around carbon Mira variables ⋆

M. A. T. Groenewegen[1], P. A. Whitelock[2], C. H. Smith[3], F. Kerschbaum[4]
[1] *Max-Planck-Institut für Astrophysik, Karl-Schwarzschild-Straße 1, D-85740 Garching, Germany (e-mail: groen@mpa-garching.mpg.de)*
[2] *South African Astronomical Observatory, P.O. Box 9, 7935 Observatory, South Africa*
[3] *Dept. of Physics, University College, ADFA, Canberra ACT 2600, Australia*
[4] *Institut für Astronomie der Universität Wien, Türkenschanzstraße 17, A-1180 Wien, Austria*

Accepted 1997. Received 1997; in original form 1997

ABSTRACT

The spectral energy distributions and mid-infrared spectra of 44 carbon Mira variables are fitted using a dust radiative transfer model. The pulsation periods of these stars cover the entire range observed for carbon Miras. The luminosities are derived from a period-luminosity relation. Parameters derived are the distance, the temperature of the dust at the inner radius, the dust mass-loss rate and the ratio of silicon carbide to amorphous carbon dust. The total mass-loss rate is derived from a modified relation between the photon momentum transfer rate (L/c) and the momentum transfer rate of the wind ($\dot{M}\ v_\infty$). Mass-loss rates between 1×10^{-8} and 4×10^{-5} $M_\odot\,yr^{-1}$ are found. We find good correlations between mass-loss rate and pulsation period ($\log \dot{M} = 4.08\ \log P - 16.54$), and mass-loss rate and luminosity ($\log \dot{M} = 3.94\ \log L - 20.79$). These relations are not independent as we assumed a $P - L$-relation. If we had assumed a constant luminosity for all stars there still would be a significant relation between $\dot{M}$ and P. The dust-to-gas ratio appears to be almost constant up to periods of about 500 days, corresponding to about 7900 $L_\odot$, and then to increase by a factor of 5 towards longer periods and higher luminosities. A comparison is made with radiation-hydrodynamical calculations including dust formation. The mass-loss rates predicted by these models are consistent with those derived in this paper. The main discrepancy is in the predicted expansion velocities for models with luminosities below ∼5000 $L_\odot$. The radiation-hydrodynamical calculations predict expansion velocities which are significantly too large. This is related to the fact that these models need to be calculated with a large C/O ratio to get an outflow in the first place. Such a large C/O ratio is contrary to observational evidence. It indicates that a principle physical ingredient in these radiation-hydrodynamical calculations is still missing. Possibly the winds are "clumpy" which may lead to dust formation on a local scale, or there is an additional outwards directed force, possibly radiation pressure on molecules.

Key words: Stars: carbon - Circumstellar matter - Stars: mass loss - stars: AGB - Infrared: stars

1 INTRODUCTION

One of the main characteristics of AGB stars is their large mass-loss rate. Dust grains form in the cool expanding circumstellar envelope, absorb optical radiation and re-emit it in the infrared. Most previous studies of dust shells around AGB stars concentrated on oxygen-rich Miras and OH/IR stars (e.g. Rowan-Robinson & Harris 1983a, Bedijn 1987, Schutte & Tielens 1989, Justtanont & Tielens 1992, Griffin 1993, Le Sidaner & Le Bertre 1993) or on the well-known carbon star IRC +10 216 (e.g. Mitchell & Robinson 1980, Martin & Rogers 1987, Le Bertre 1987, Orofino et al. 1990, Griffin 1990, Danchi et al. 1994, Winters et al. 1994, Bagnulo et al. 1995, Ivezić & Elitzur 1996, Groenewegen 1997a).

Rowan-Robinson & Harris (1983b) considered a sample of 44 carbon stars but no IRAS and LRS data were available at the time. Rowan-Robinson et al. (1986) fitted the spec-

⋆ Based on observations obtained with the UKIRT, Hawaii, U.S.A.. The United Kingdom Infrared Telescope is operated by the Royal Observatory Edinburgh on behalf of the U.K. Science and Engineering Research Council. Based on observations made with the Carlos Sanchez telescope operated on the island of Tenerife in the Spanish Observatorio del Teide of the Instituto de Astrofísica de Canarias.

tral energy distributions (SEDs) of five carbon stars, fixing the dust temperature at the inner radius at 1000 K. They also assumed a dust absorption law of $\sim\lambda^{-1}$ for all wavelengths, without considering the presence of silicon carbide (SiC), which has a feature near 11.3 μm. Le Bertre (1988b) fitted three carbon stars. Chan & Kwok (1990) fitted SEDs of 145 carbon stars with an LRS classification of 4n (indicating silicon carbide emission), and they therefore missed some carbon stars with weak silicon carbide emission (which sometimes have an LRS = 1n classification) and extreme carbon stars which have an LRS = 2n classification. They fixed the dust temperature at the inner radius at 1500 K and only included silicon carbide dust in their model. Lorentz-Martins & Lefévre (1993, 1994) fitted nine and 32 carbon stars, respectively. In the 1993 paper they used the same inner radius for both SiC and amorphous carbon (AMC) grains. In the 1994 paper they allowed for different inner radii for the two dust species. In a recent paper Lorentz-Martins (1996) fitted 8 J-type carbon stars.

In Groenewegen (1995a, hereafter G95) the SEDs and LRS spectra of 21 carbon stars were fitted, concentrating on "infrared" carbon stars, i.e. those with thick dust shells. Different types of silicon carbide were tested and it was concluded that in 18 of 21 cases α-SiC fitted the observed feature. The inner radius for SiC and for AMC was taken to be identical. In agreement with the results of Lorentz-Martins & Lefévre (1993, 1994) it was found that the ratio SiC/AMC decreases with increasing optical depth of the shell.

In the present paper we concentrate on carbon-rich Mira variables (from now on we mean carbon-rich Miras by the term Miras unless otherwise noted). The main advantage of using Miras is that the period-luminosity relation provides reasonable accurate distances for such stars, largely eliminating the uncertainty of some of the fit parameters on distance. Secondly, using Miras enables a study to be made of the relation between mass-loss rate and pulsation period, c.q. mass-loss rate and luminosity, which is important from an evolutionary point of view. To this end we took the 10 stars from G95 with measured pulsation periods and selected 34 other stars from the literature to cover the entire known range of periods for Miras.

As preliminary results indicated that the mass-loss rate of Miras with periods below 400 days may be lower than expected from an extrapolation of the results for longer periods (Groenewegen 1995b, 1995c) emphasis was put on the selection of short period Miras.

The paper is organised as follows. In Sect. 2 the radiative transfer model is introduced. In Sect. 3 the Period–Luminosity relation is presented. In Sect. 4 new observations are discussed. In Sect. 5 the fits to the SEDs and LRS spectra are presented. In Sect. 6 the final values of the mass-loss rate and dust-to-gas ratio are derived and the results are discussed in Sect. 7.

2 THE MODEL

The radiative transfer model of Groenewegen (1993) is used. This model was developed to handle non-r^{-2} density distributions in spherically symmetric dust shells. It simultaneously solves the radiative transfer equation and the thermal balance equation for the dust.

When the input spectrum of the central source is fixed, the shape of the SED is exclusively determined by the dust optical depth, defined by:

$$\tau_\lambda = \int_{r_{\rm inner}}^{r_{\rm outer}} \pi a^2 Q_\lambda \, n_d(r) \, dr =$$

$$= 5.405 \times 10^8 \, \frac{\dot{M} \, \Psi \, Q_\lambda / a}{R_\star \, v_\infty \, \rho_d \, r_c} \int_1^{x_{\rm max}} \frac{R(x)}{x^2 w(x)} \, dx \qquad (1)$$

where $x = r/r_c$, $\dot{M}(\mathrm{r}) = \dot{M} \, R(x)$ and $v(r) = v_\infty \, w(x)$. The normalized mass-loss rate profile $R(x)$ and the normalized velocity law $w(x)$ should obey $R(1) = 1$ and $w(\infty) = 1$, respectively. In the case of a constant mass-loss rate and a constant velocity, the integral in Eq. (1) is essentially unity since $x_{\rm max}$ is always much larger than 1. The symbols and units in Eq. (1) are: the (present-day) mass-loss rate $\dot{M}$ in $\mathrm{M}_\odot\,\mathrm{yr}^{-1}$, Ψ the dust-to-gas mass ratio (assumed constant with radius), Q_λ the extinction coefficient, a the grain size in cm (the model assumes a single grain size), $R_\star$ the stellar radius in $R_\odot$, v_∞ the terminal velocity of the dust in km s^{-1}, $\rho_{\rm d}$ the dust grain specific density in g cm^{-3}, $r_{\rm c}$ the inner dust radius in units of stellar radii and $x_{\rm max}$ the outer radius in units of $r_{\rm c}$. It should be noted that from the model fitting only the dust mass-loss rate can be determined, i.e. $\dot{M} \times \Psi$.

In a detailed study of IRC +10 216 (Groenewegen 1997a) it was found that including a velocity law to calculate the density (i.e. $\frac{1}{r^2 \, v(r)}$) gave somewhat worse results that using a simple r^{-2} law. It was argued that since the dust-to-gas ratio is also an increasing function of radius the two effects tend to cancel. Fully consistent models (Winters 1994) lend some support to this idea. A constant velocity is therefore assumed as well as a constant mass-loss rate. On the other hand, if some specific velocity law would be adopted then this would simply lead to a rescaling of the mass loss rate in such a way as to obtain the same optical depth as with a constant velocity.

Unless otherwise specified the outer radius is determined in the model by a dust temperature of 20 K and a grain specific density of $\rho_{\rm d} = 2.0$ g cm^{-3} is adopted.

In most models the terminal velocity of the dust is assumed to be equal to that of the gas. This, however, neglects the drift velocity of the dust with respect to the gas, ($v_{\rm dust} = v_{\rm gas} + v_{\rm drift}$), which may be estimated from (e.g. Kwan & Hill 1977):

$$v_{\rm drift} = 1.43 \times 10^{-4} \; \mathrm{km\,s^{-1}} \left(\frac{L \, Q_{\rm F}(r) \, v_\infty^{\rm gas}}{\dot{M}} \right)^{0.5} \qquad (2)$$

where $v_\infty^{\rm gas}$ is the terminal velocity of the gas, with L the stellar luminosity in solar units and $Q_{\rm F}(r)$ the flux-weighted extinction coefficient, defined as $Q_{\rm F}(r) = \frac{\int F_\lambda(r) \, Q_\lambda \, d\lambda}{\int F_\lambda(r) \, d\lambda}$. In Sect. 6 the influence of the drift velocity on the mass-loss rates is discussed.

The central star is represented by a blackbody modified to allow for the characteristic absorption feature in carbon stars at 3.1 μm due to HCN and C_2H_2 (e.g. Ridgway et al. 1978):

$$B_\lambda(T_{\rm eff}) \; \exp\left(-A \; e^{-\left(\frac{\lambda - \lambda_0}{\Delta\lambda}\right)^2} \right) \qquad (3)$$

Table 1. SAAO Near-infrared photometry

JD-2440000	J	H	K	L	Tel.
		ZZ Gem			
8586.52	5.08	3.71	3.03	2.46	0.75
8629.39	5.58	4.10	3.26	2.61	0.75
8668.32	5.80	4.34	3.39	2.72	0.75
8965.50	5.54	4.03	3.20	2.48	0.75
8986.43	5.58	4.10	3.26	2.59	0.75
9061.25	5.08	3.86	3.22	2.69	0.75
9382.37	5.02	3.79	3.16	2.64	0.75
9639.63	5.56	4.14	3.30	2.73	0.75
9672.55	5.31	4.01	3.26	2.74	0.75
		RT Gem			
8586.56	6.15	4.86	4.33	3.85	0.75
8633.39	6.58	5.26	4.61	4.22	0.75
8669.33	6.90	5.58	4.87	4.53	0.75
8965.53	6.31	5.02	4.47	4.02	0.75
8986.47	6.49	5.18	4.60	4.21	0.75
9061.29	6.65	5.48	4.90	4.54	0.75
9376.35	6.80	5.56	4.89	4.57	1.9
9639.65	6.13	4.84	4.36	3.96	0.75
9672.57	6.36	5.09	4.52	4.13	0.75
		R CMi			
2036.50	3.58	2.62	2.24	1.90	1.0
5007.39	4.13	3.15	2.78	2.36	0.75
5688.48	4.09	3.14	2.75	2.43	0.75
8589.55	4.58	3.48	2.92	2.71	0.75
8632.46	4.40	3.35	2.91	2.61	0.75
8669.35	4.24	3.22	2.84	2.51	0.75
8962.53	4.32	3.24	2.83	2.43	0.75
8987.47	4.26	3.21	2.81	2.37	0.75
9056.30	3.67	2.60	2.25	1.78	0.75
9376.34	3.93	2.90	2.51	2.16	1.9
9642.63	4.34	3.30	2.87	2.43	0.75
9672.58	4.14	3.13	2.77	2.34	0.75
		VX Gem			
8589.56	5.14	3.82	3.10	2.68	0.75
8633.40	5.47	4.16	3.33	2.97	0.75
8669.34	5.61	4.34	3.49	3.18	0.75
8962.54	4.96	3.65	3.00	2.62	0.75
8986.50	5.15	3.82	3.11	2.74	0.75
9058.27	5.43	4.17	3.38	3.06	0.75
9376.36	5.19	3.86	3.14	2.74	1.9
9641.65	4.37	3.22	2.82	2.47	0.75
9673.58	4.46	3.25	2.81	2.37	0.75
		TV Vel			
2035.50	5.23	3.99	3.18	2.96	0.75
2552.50	5.03	3.90	3.26	2.97	0.75
3515.55	5.02	3.87	3.38	2.80	0.75
4336.40	4.98	3.84	3.30	2.79	0.75
8665.56	5.16	3.97	3.38	2.86	0.75
8735.37	5.11	3.90	3.42	2.87	0.75
8967.57	5.26	3.88	3.14	2.73	0.75
9001.44	5.47	4.12	3.31	2.86	0.75
9061.44	5.39	4.13	3.42	3.01	0.75
9107.33	5.11	3.93	3.38	2.85	0.75
9173.22	5.10	3.91	3.43	2.86	0.75
9379.57	5.22	3.87	3.12	2.62	0.75
9403.48	5.37	4.00	3.23	2.83	0.75
9677.57	4.68	3.46	3.02	2.50	0.75

Table 1. Continued

JD-2440000	J	H	K	L	Tel.
		R Cap			
2551.50	5.79	4.33	3.30	2.06	0.75
2593.50	6.30	4.64	3.54	2.37	0.75
8786.60	5.52	3.98	3.02	1.98	0.75
8876.37	6.17	4.64	3.52	2.64	0.75
9146.56	5.46	3.96	3.05	2.13	0.75
9213.48	5.91	4.40	3.38	2.55	0.75
9231.37	5.83	4.37	3.38	2.56	0.75
9639.33	5.87	4.21	3.28	2.40	0.75
9673.25	5.09	3.85	3.04	2.10	0.75

with λ_0 = 3.1 μm. This novelty is introduced to enable a direct fit to the observed 2-4 μm spectra of some stars. Following Groenewegen et al. (1994) values of A = 4.605 and $\Delta\lambda$ = 0.075 μm are adopted. This value of A provides a flux in the 3.1 μm feature which is 1% of the continuum in a star without a circumstellar shell.

For the dust composition a combination of amorphous carbon (AMC) and silicon carbide (SiC) grains is assumed. For simplicity a single condensation temperature is used. In principle SiC and AMC could have different temperature profiles but to take this into account requires two additional free parameters (a second condensation temperature and dust-to-gas ratio). Since the abundance of SiC is found to be small, the simplification of the temperature profile seems to be justified. In Eq. (1) the value of (Q_λ/a) is calculated from $(Q_\lambda/a) = x\ (Q_\lambda/a)^{SiC} + (1-x)\ (Q_\lambda/a)^{AMC}$ where x ($\in [0,1]$) is determined by the fit to the LRS spectrum. The absorption coefficient for AMC is calculated from the optical constants listed in Rouleau & Martin (1991) for their AC1-species.

It was shown in G95 that most of the silicon carbide features can be fitted with α-SiC (Pégourié 1988). The optical constants from that paper are therefore adopted.

Beam effects are taken into account. This is especially important for longer wavelengths ($\lambda \gtrsim 50$ μm) where the emission becomes extended relative to the typical beams used in far-infrared observations. In particular, for $\lambda < 7$ μm a Gaussian beam with a FWHM (full width half maximum) of 20$''$ is assumed (typical of near-infrared observations). Between 7 μm $< \lambda <$ 140 μm the beam effects of the IRAS detectors are taken into account (for details see Groenewegen 1993). For $\lambda >$ 140 μm a Gaussian beam of FWHM = 18.5$''$ is assumed, representative of the far-IR observations to which the model is compared.

In the models the calculated energy distribution is convolved with the spectral response of the IRAS filters (Table II.C.5 of the Explanatory Supplement) to compare the predicted flux-densities directly to the flux-densities listed in the IRAS Point Source or Faint Source Catalogs.

Table 2. The program stars

IRAS-name	GCVS	Period[(a)] (days)	$\Delta K^{(b)}$ (mag)	Lum. ($L_\odot$)	l	b	A_V (mag)	$v_\infty{}^{(c)}$ (kms^{-1})	photometry[(d)]
01144+6658	–	1060 (5)	2.4	16380	125.5	4.5	2.5	18.1 (2)	16, 29, 39, 48, 53
02032+5636	CN Per	384 (1)	–	5720	133.1	−44.5	1.8	(10:) (6)	61
02270−2619	R For	388.7 (1)	0.84	5790	215.8	−68.1	0.1	16.9 (3)	6,20,30,36,37,53,54,58
02293+5749	–	815 (5)	2.5	12470	136.1	−2.2	3.0	14.2 (1)	16, 20, 29, 53
03229+4721	V384 Per	535 (1)	1.4	8060	148.2	−7.6	1.1	15.5 (2)	4, 10, 22, 30, 41
03243+4400	Y Per	252.3 (4)	–	3700	150.3	−10.2	1.0	7.2 (3)	3, 5, 30, 49
03488+3943	V414 Per	515 (2)	1.0	7750	156.6	−10.9	1.1	30.7 (2)	27, 30, 41, 48, 53
04562+0803	R Ori	378.0 (4)	0.7	5630	191.7	−20.5	0.4	10(:) (3)	3, 6, 30, 58
04573−1452	R Lep	427.1 (1)	0.6	6380	214.3	−31.3	0.2	19.0 (1)	7,18,26,30,32,33,37,50,53,58
05185+3227	UV Aur	394.4 (1)	0.67	5880	174.2	−2.4	1.0	(10:) (6)	30, 46, 50, 51, 53, 60
06012+0328	V1259 Ori	696 (3)	1.73	10590	200.8	−7.0	1.3	16.5 (2)	22, 27, 37
06202+4743	V Aur	353 (1)	–	5240	166.8	15.4	0.7	20(:) (3)	3, 4, 30
06209+2503	ZZ Gem	317.0 (1)	0.33	4690	187.6	5.5	1.6	6.8 (3)	5, 10, 30, 47, 50, 61
06230−0930	–	494 (3)	1.40	7430	218.6	−10.1	1.5	16.6 (3)	8, 20, 21, 37, 53
06342+0328	V688 Mon	653 (3)	1.48	9910	208.2	−1.7	2.7	13.3 (1,3)	20, 21, 22, 25, 37
06436+1840	RT Gem	350.4 (1)	0.57	5200	195.7	7.3	1.0	(10:) (6)	61
06529+0626	CL Mon	497.2 (1)	0.7	7470	207.7	3.8	0.8	26.1 (1,3)	13, 30, 50, 53, 58
07059+1006	R CMi	337.8 (1)	0.68	5010	205.9	8.4	0.8	(10:) (6)	3,6,18,26,30,40,50,53,58,61
07065−7256	R Vol	453.6 (1)	0.9	6800	284.2	−24.8	0.5	20.3 (1,3)	6, 13, 15, 30, 53, 58
07098−2012	–	725 (3)	1.30	11050	233.3	−4.8	1.0	24.0 (1,2)	21, 22, 37
07099+1441	VX Gem	379.4 (1)	0.68	5650	202.2	11.3	0.6	(10:) (6)	30, 50, 53, 61
08434−2801	R Pyx	364.7 (1)	–	5420	251.3	9.2	0.9	8.8 (3)	6, 13, 30, 58
09452+1330	CW Leo	630 (2,3)	2.03	9550	221.5	45.1	0.1	14.5 (1,2)	24
10324−5358	TV Vel	365.2 (1)	0.40	5430	283.7	3.4	1.0	(10:) (6)	61
12447+0425	RU Vir	433.2 (1)	1.0	6480	300.3	67.0	0.1	15.4 (2)	6,11,15,17,19,30,45,50,53
12536−5737	V Cru	376.5 (1)	0.4	5600	303.6	5.0	1.4	(10:) (6)	6, 30, 58, 59
15194−5115	–	580 (3)	1.16	8770	325.5	4.7	0.8	22.2 (4)	12, 22, 37, 44, 52
15477+3943	V CrB	357.6 (1)	–	5310	63.3	51.2	0.1	8.1 (3)	2, 4, 14, 18, 26, 30, 53, 55
16239−1218	V Oph	297.2 (1)	0.54	4390	3.0	24.5	0.6	7.0 (3)	18, 20, 28, 30, 31, 34, 50, 53
17556+5813	T Dra	421.6 (1)	–	6300	86.8	29.9	0.1	13.1 (1)	14, 17, 18, 26, 50, 53
19008+0726	–	577 (3)	1.32	8720	41.0	0.8	1.6	26.0 (3)	37, 47, 50, 53
19175−0807	–	676 (3)	1.41	10280	29.0	−10.1	0.9	27.5 (3)	8, 22, 27, 37, 53

3 PERIOD-LUMINOSITY RELATION

To estimate the luminosity from the pulsation periods we use the period-luminosity relation from Groenewegen & Whitelock (1996):

$$M_{\rm bol} = -2.59 \log P + 2.02. \quad (4)$$

This relation was derived for carbon Miras in the Large Magellanic Cloud and was shifted by the distance modulus of 18.5 mag to get the $P-L$-relation for carbon Miras in our Galaxy. The relation was derived for periods below 520 days, but new data for likely carbon-rich Miras with periods up to 900 days in the LMC appear to lie on an extrapolation (Groenewegen et al. 1997). Therefore, Eq. (4) is used for all periods to obtain the luminosity (Tab. 2, column 5).

The derived distances and dust mass-loss rates (see Tab. 2) depend on the assumed luminosity so that $D \propto \sqrt{L}$, and $\dot{M} \propto \sqrt{L}$.

4 OBSERVATIONS

The models are fitted to the observed SEDs and mid-IR spectra. Most of these data come from the literature (see column 10 in Tab. 2). However, some new or previously unpublished data are also used as constraints, in particular for some of the stars with few published photometric, or poor mid-IR spectroscopic data.

Mid-infrared spectra of R CMi, TV Vel, V Cru, VX Gem, ZZ Gem and R Ori were taken on November 25–27, 1994 with the UCL IR cooled grating array spectrometer (for details see Aitken & Roche 1982) mounted at the f/36 Cassegrain focus of the 3.9m Anglo-Australian Telescope. We used a circular aperture of 4.2$''$ diameter, while the (optical) seeing was in the range 1.0–1.5$''$ for most of the time. The 8.0 to 13.0 μm window was covered with 25 detectors, resulting in an effective resolution of $\lambda/\Delta\lambda \approx 50$. The grating was stepped once, offset by one and a half detector widths, providing an oversampled (50 data point) spectrum, which was subsequently smoothed. Chopping, with a frequency of 12.5 Hz, and beam-switching were employed, each using a throw of 15$''$ in declination. The pointing of the telescope was regularly verified on a bright nearby star. The observations were obtained through cirrus clouds which is reflected by the large error bars. Flux calibration and correction for telluric absorption were made by reference to the F0II star α Car.

Mid-infrared spectra were obtained of RT Gem on January 12, 1995, of V Aur and R CMi on January 14, 1995, and of CN Per and UV Aur on August 21, 1995, respectively. The common-user instrument CGS3 was used at the 3.8m

Table 2. Continued

IRAS-name	GCVS	Period[(a)] (days)	$\Delta K^{(b)}$ (mag)	Lum. ($L_\odot$)	l	b	A_V (mag)	v_∞[(c)] (kms^{-1})	photometry[(d)]
19321+2757	V1965 Cyg	625 (2)	1.9	9470	62.6	4.0	1.5	26.0 (1,2)	20, 22, 27, 50
19594+4047	V1968 Cyg	783 (2)	1.6	11970	76.5	5.6	1.2	21.5 (2)	1, 22, 23, 27, 43
20072+3116	V1969 Cyg	550 (2)	1.9	8300	69.4	−0.9	2.3	25.6 (2)	8, 22, 27, 43, 53
20085−1425	R Cap	345.2 (1)	0.54	5120	28.6	−24.0	0.3	10.5 (3)	8, 25, 30, 61
20396+4757	V Cyg	421 (1)	–	6290	86.5	3.8	0.9	13.2 (1)	2, 4, 20, 22, 30, 35
20570+2714	–	750 (2)	1.6	11440	72.6	−12.0	0.8	25.8 (3)	8, 9, 19, 27, 53
21035+5136	V1549 Cyg	533 (2)	1.4	8030	91.8	3.2	1.2	11.4 (1)	8, 10, 27, 42, 50, 53, 56
21262+7000	AX Cep	395 (1)	–	5890	107.2	13.9	1.2	13.2 (2)	30, 47, 53
21320+3850	V1426 Cyg	470 (1)	∼0.8	7050	86.3	−9.4	0.9	13.9 (1,2)	10, 20, 26, 30, 50, 53
22036+3315	RZ Peg	438.7 (1)	–	6570	87.6	−17.8	0.5	12.6 (5)	3, 30, 32, 50, 51
23166+1655	–	696 (3)	1.90	10590	93.5	−40.4	0.1	14.6 (1,2)	22, 23, 27, 37, 38, 52, 57
23320+4316	LP And	620 (2)	2.1	9400	108.5	−17.1	0.5	14.7 (1,2)	8, 20, 22, 27, 30, 41

(a) Between parentheses the references for the pulsation period: 1 = GCVS (Kholopov et al. 1985), 2 = Jones et al. (1990), 3 = Le Bertre (1992), 4 = SIMBAD database, 5 = Joyce et al. 1997.
(b) Full amplitude in the K-band.
(c) Between parentheses the references for the gas expansion velocity: 1 = average of values in Loup et al. (1993), 2 = Groenewegen et al. (1996a), 3 = Groenewegen et al. (1996b), 4 = Nyman et al. (1993b), (5) Sahai & Liechti (1995), (6) = not available, a value of 10 km s^{-1} has been adopted. Uncertain values are indicated by a (:).
(d) References for the photometry used: 1 = Alknis (1980), 2 = Altenhoff et al. (1994), 3 = Barnes (1973), 4 = Bergeat et al. (1976), 5 = Bergeat & Lunel (1980), 6 = Catchpole et al. (1979), 7 = Celis (1982), 8 = Cohen & Kuhi (1977), 9 = Cohen (1984), 10 = Dyck et al. (1974), 11 = Eggen (1975), 12 = Epchtein et al. (1987), 13 = Epchtein et al. (1990), 14 = Forrest et al. (1975), 15 = Fouqué et al. (1992), 16 = Gehrz & Hackwell (1976), 17 = Gehrz et al. (1984), 18 = Gillett et al. (1971), 19 = Gosnell (1979), 20 = Grasdalen et al. (1983), 21 = Groenewegen & de Jong (1993), 22 = Groenewegen et al. (1993), 23 = Groenewegen et al. (1994), 24 = Groenewegen (1997a), 25 = Guglielmo et al. (1993), 26 = Hackwell (1972), 27 = Jones et al. (1990), 28 = Jørgensen & Westerlund (1988), 29 = Joyce et al. (1997), 30 = Kholopov et al. (1985), 31 = Landolt (1968), 32 = Landolt (1969a), 33 = Landolt (1969b), 34 = Landolt (1973), 35 = Lázaro et al. (1994), 36 = Le Bertre (1988a), 37 = Le Bertre (1992), 38 = Lebofsky & Rieke (1977), 39 = Lebofsky et al. (1978), 40 = Lockwood (1972), 41 = Lockwood (1974), 42 = Lockwood (1985), 43 = Low et al. (1976), 44 = Meadows et al. (1987), 45 = Merrill & Stein (1976), 46 = Munari et al. (1992), 47 = Neugebauer & Leighton (1969), 48 = Ney & Merrill (1980), 49 = Nicolet (1978), 50 = Noguchi et al. (1981), 51 = Olson & Richer (1975), 52 = Omont et al. (1996), 53 = Price & Murdock (1983), 54 = Richer (1971), 55 = Simon (1976), 56 = Strecker & Ney (1974), 57 = Sopka et al. (1985), 58 = Walker (1979), 59 = Whitelock et al. (1997), 60 = Woolf (1973), 61 = This paper (Sect. 4)
In addition the IRAS PSC or FSC flux-densities and the LRS spectra (when available), corrected according to Cohen et al. (1992), are used, or newly obtained mid-IR spectra (see Sect. 4).

UKIRT telescope under photometric conditions during service observing. The spectra were wavelength calibrated using a Kr lamp; the accuracy of the fit is 0.01 μm rms. Flux calibration and correction for telluric absorption were made by reference to BS 1708 (UV Aur, V Aur, CN Per) and BS 2990 (RT Gem, R CMi).

Table 1 lists $JHKL$ magnitudes for six of the stars under discussion, obtained on the 0.75, 1.0 or 1.9-m telescopes at SAAO as specified in the table. The photometry is on the SAAO system as defined by Carter (1990). It is accurate to better than $\pm$0.03 mag at JHK and better than $\pm$0.05 mag at L. Note that a small number of the older measurements of R CMi and TV Vel were reported by Catchpole et al. (1979). The measurements listed here differ slightly from those in the earlier paper as they have been corrected to Carter's improved values for the standard stars.

CN Per was observed on August 8th, 1996 with the 1.5m Carlos Sanchez telescope at the Teide observatory on the island of Tenerife with the following result: J = 7.02, H = 5.81, K = 4.98.

5 THE FITTING PROCEDURE

In Tab. 2 some general parameters of the stars are listed. The sample is a selection of Miras, ranging from stars with low to moderate mass-loss rates to the reddest carbon stars known. The stars have been selected for the availability of as many flux determinations over as large a wavelength region as possible and cover the whole range of known Mira periods.

Table 2 lists the IRAS and GCVS-name, the pulsation period, the full amplitude in the K-band when available, the luminosity derived from Eq. (4), the galactic coordinates, the interstellar extinction in the V-band (see below), the terminal gas velocity of the envelope, and the references to the photometry used to construct the SEDs. LRS spectra are either taken from the LRS atlas (1986), or from the database available at the University of Calgary. The LRS spectra are corrected according to Cohen et al. (1992). No LRS spectra are available for Y Per, R Ori and RT Gem. Y Per is nevertheless included as it is the carbon Mira with the shortest pulsation period. For RT Gem a UKIRT 7–13 μm spectrum is available, for R Ori an AAT spectrum.

The interstellar extinction at V was estimated, either

Table 3. The fit parameters

IRAS-name	$T_{\rm inn}$ (K)	$T_{\rm eff}$ (K)	$\dot{M}_{\rm dust}^{(a)}$ ($M_{\odot}$ yr^{-1})	r$_{\rm c}$ (R_*)	x$^{(b)}$	d (kpc)	$\tau_{11.33}$	$\tau_{0.5}$	$\tau_{\rm F}$	$Q_{\rm F}^{(c)}$	remarks
01144+6658	1000	2500	9.5 10^{-7}	9.8	0.08	3.99	4.84	79.2	2.41	0.0115	AFGL 190
02032+5636	1500	2500	1.0 10^{-9}	2.0	0.08	3.09	0.076	1.24	0.29	0.0884	
02270−2619	1300	2300	4.9 10^{-9}	2.4	0.04	0.60	0.12	2.60	0.45	0.0665	AFGL 337
02293+5749	1000	2500	3.0 10^{-7}	8.3	0.08	2.55	2.62	42.9	1.74	0.0152	AFGL 341
03229+4721	1000	2500	2.5 10^{-8}	6.0	0.06	0.65	0.31	5.75	0.63	0.0408	AFGL 489
03243+4400	–	2500	0.0	–	–	1.04	0.0	0.0	0.0	0.1211	$\dot{M}$ forced to 0
03488+3943	1500	2500	1.2 10^{-8}	2.2	0.04	0.99	0.18	3.93	0.62	0.0608	AFGL 527
04562+0803	1500	2500	6.0 10^{-10}	2.0	0.05	2.22	0.038	0.86	0.20	0.1000	
04573−1452	1500	3000	4.2 10^{-9}	3.3	0.08	0.42	0.14	2.31	0.49	0.0789	AFGL 667
05185+3227	1500	3000	1.0 10^{-9}	3.1	0.06	0.85	0.061	1.15	0.32	0.1025	AFGL 735
06012+0328	800	2500	2.4 10^{-7}	12.0	0.02	1.45	0.89	23.2	1.06	0.0173	AFGL 865
06202+4743	1500	2500	3.0 10^{-10}	1.9	0.25	1.16	0.025	0.18	0.058	0.1029	
06209+2503	1500	2500	8.5 10^{-11}	1.9	0.10	1.32	0.013	0.20	0.057	0.1130	
06230−0930	1200	2500	2.7 10^{-8}	4.1	0.05	2.00	0.43	8.71	0.85	0.0362	AFGL 935
06342+0328	1100	2500	4.2 10^{-8}	5.3	0.05	1.55	0.58	11.7	0.90	0.0294	AFGL 971
06436+1840	–	2800	0.0	–	–	0.91	0.0	0.0	0.0	0.1319	$\dot{M}$ forced to 0
06529+0626	1500	2500	4.7 10^{-9}	2.1	0.08	0.82	0.12	1.89	0.40	0.0790	AFGL 1038
07059+1006	1500	2700	2.0 10^{-10}	2.3	0.08	0.86	0.016	0.27	0.086	0.1176	
07065−7256	1400	2500	1.1 10^{-8}	2.6	0.07	0.75	0.26	4.55	0.67	0.0544	AFGL 4070
07098−2012	1000	2500	6.0 10^{-8}	6.2	0.05	1.63	0.37	7.46	0.69	0.0353	AFGL 1085
07099+1441	1500	2500	8.0 10^{-10}	2.0	0.15	1.62	0.087	0.96	0.25	0.0908	
08434−2801	600	2500	8.0 10^{-10}	19.2	0.12	1.20	0.0091	0.12	0.033	0.1000	
09452+1330	1075	2000	7.5 10^{-8}	4.5	0.03	0.15	0.62	84.8	0.97	0.0261	$a = 0.16$ μm
10324−5358	1500	2700	6.5 10^{-10}	2.4	0.08	1.54	0.050	0.82	0.23	0.1023	
12447+0425	1500	2500	5.0 10^{-9}	2.2	0.08	0.75	0.21	3.51	0.59	0.0627	AFGL 1579
12536−5737	1500	2700	3.0 10^{-10}	2.3	0.10	1.33	0.026	0.37	0.12	0.1133	
15194−5115	1050	2500	8.0 10^{-8}	7.1	0.02	0.63	0.41	67.8	0.80	0.0293	$a = 0.10$ μm
15477+3943	1000	2500	1.5 10^{-9}	5.4	0.07	0.71	0.052	0.99	0.22	0.0920	AFGL 5311
16239−1218	1500	2700	8.5 10^{-11}	2.3	0.15	0.68	0.015	0.17	0.057	0.1169	AFGL 1859
17556+5813	1200	2500	9.5 10^{-9}	3.8	0.06	0.73	0.25	4.62	0.63	0.0503	AFGL 2040
19008+0726	1200	2500	7.0 10^{-8}	4.4	0.03	0.81	0.53	12.7	0.98	0.0301	AFGL 2310
19175−0807	1100	2500	8.0 10^{-8}	5.2	0.04	0.88	0.49	10.8	0.88	0.0308	AFGL 2368
19321+2757	900	2500	7.0 10^{-8}	7.9	0.03	1.11	0.29	6.90	0.64	0.0352	AFGL 2417
19594+4047	900	2500	2.0 10^{-7}	8.9	0.05	1.84	0.90	18.1	1.02	0.0208	AFGL 2494
20072+3116	1200	2500	1.1 10^{-7}	4.7	0.05	1.20	0.95	19.2	1.23	0.0244	AFGL 2513
20085−1425	1200	2500	3.9 10^{-9}	3.6	0.10	1.47	0.19	2.96	0.47	0.0645	
20396+4757	1200	2500	1.1 10^{-8}	3.8	0.06	0.40	0.29	5.24	0.71	0.0471	AFGL 2632
20570+2714	900	2500	1.1 10^{-7}	8.1	0.03	1.08	0.39	9.20	0.72	0.0297	AFGL 2686
21035+5136	1100	2500	1.5 10^{-8}	4.8	0.06	1.32	0.31	5.89	0.67	0.0422	AFGL 2704
21262+7000	1500	3000	5.0 10^{-9}	3.5	0.08	1.05	0.24	4.28	0.63	0.0618	AFGL 2768
21320+3850	1050	2500	1.5 10^{-8}	5.2	0.06	0.72	0.25	4.71	0.59	0.0467	CIT 13
22036+3315	1200	2600	5.0 10^{-10}	3.7	0.03	1.23	0.011	0.28	0.085	0.1148	
23166+1655	650	2500	5.5 10^{-7}	20.4	0.00	1.15	1.12	36.0	1.11	0.0121	AFGL 3068
23320+4316	900	2500	8.0 10^{-8}	8.5	0.03	0.71	0.55	13.0	0.84	0.0247	AFGL 3116

(a). Dust mass rate assuming a dust opacity at 60 μm of 68 cm^{2}gr^{-1} and a dust velocity equal to the gas velocity.
(b). x is the mass ratio of SiC to AMC (see Sect. 2.)
(b). For $a = 0.1$ μm, and scales like $Q_{\rm F} \sim a$.

from Neckel & Klare (1980) (who list observed values of $A_{\rm V}$ as a function of galactic coordinates and distance) for stars with $\mid b \mid \lesssim 7.6^0$, or from Burnstein & Heiles (1982) for those with $\mid b \mid \gtrsim 10^0$. Parenago's (1940) model was used for those stars outside of the range covered by these two papers and to obtain a second estimate for those in range (see Groenewegen et al. 1992 for the exact form). The estimates of $A_{\rm V}$ usually agree and the adopted values are listed in Tab. 2.

The fitting procedure is as follows. Typically four values for the dust temperature at the inner radius ($T_{\rm inn}$) are chosen. The mass-loss rate (assumed constant) is varied to fit the (shape of the) SED and mid-infrared spectra. The distance is determined by demanding that the predicted and observed mean near-infrared magnitudes agree. The SiC feature is fitted by changing the (mass) ratio SiC/AMC. This last step is straightforward since the strength of the SiC feature turns out to scale linearly with the adopted SiC/AMC ratio. In choosing the best value for $T_{\rm inn}$ equal weight is given to the fits of the SED and the LRS spectrum. If necessary, the afore mentioned steps are repeated for the final choice of $T_{\rm inn}$. For most stars the default value of 2500 K for the effective temperature of the central star gives good results. For some stars a different value gives better results. The formal errors in the mass-loss rate and $T_{\rm inn}$ are estimated to be 20% (3σ).

For two stars interferometric visibility curves are fitted as well. IRC +10 216 is discussed in detail in Groenewegen (1997a). A best fitting grain size of 0.16 μm was derived. For IRAS 15194–5115 the $K-$ and $L-$band visibility curves as presented by Lopez et al. (1993) were fitted. A best fitting grain size of 0.10 μm is derived.

The best-fitting models are shown in Figs. 6 to 48, except that of CW Leo which is extensively discussed in Groenewegen (1997a). The spectra have been corrected for interstellar extinction using A_V from Tab. 2 and the interstellar extinction curve of Cardelli et al. (1988). The corresponding model parameters are included in Tab. 3 which lists the IRAS name, the temperature of the dust at the inner radius, the effective temperature of the central stars, the dust mass-loss rate (assuming the standard values for the dust opacity dust-to-gas ratio and furthermore assuming that the dust velocity equals the gas velocity, thereby neglecting the drift velocity; see Sect. 6), the inner dust radius, the ratio of silicon carbide to amorphous carbon, the derived distance for the assumed luminosity from Tab. 2, the optical depth at 11.33 and 0.5 μm, the flux-weighted optical depth (defined as $\tau_{\rm F}(r) = \frac{\int F_\lambda(r)\ \tau_\lambda\ d\lambda}{\int F_\lambda(r)\ d\lambda}$), the flux-weighted extinction coefficient for a grain size of 0.1 μm and a remarks column which usually gives the number in the AFGL catalog, as an alternative for the GCVS name listed in Tab. 2.

The derived dust mass-loss rates are subject to the following systematic effects. Following Eq. (1) the mass-loss rate scales like $\sim R_\star\, v_\infty / \kappa_\lambda$, where κ_λ is the dust opacity. For a constant effective temperature, the derived dust mass-loss rates (and derived distances) scale like $\sqrt{L}$. The opacity at 60 μm for the adopted absorption coefficient ($\kappa = 3\ Q/4\ a\ \rho_d$) is 68 cm^{2}gr^{-1}. This is about a factor of 2 lower than the usually quoted value of $\sim$160 cm^{2}gr^{-1} (see, e.g. Jura 1986). Since the mass-loss rate scales like κ^{-1}, the values quoted in Table 3 may be systematically too high by about a factor of 2.

The fits to the SEDs and mid-IR spectra are generally of good quality. Problems can arise when there is little observational data (e.g. CN Per; Fig. 7). The bad fits may in some cases also be due to the simple blackbody approximation for the emission from the central star, in particular when the mass-loss rate is small and the photospheric contribution to the total flux becomes important.

As found in G95, the α-SiC opacity provides good fits to the observed features in most cases. When it does not, the observed feature peaks at shorter wavelengths (e.g. AFGL 489 [Fig. 10], R Lep [Fig. 14]). A special case is that of the reddest stars, like AFGL 190 and AFGL 3068. There have been claims that the SiC feature goes into absorption (Jones et al. 1978, Lequeux & Jourdain de Muizon 1990, Justtanont et al. 1996) for such stars. For comparison, AFGL 3068 (Fig. 40) is fitted with pure amorphous carbon, while for AFGL 190 (Fig. 5) an attempt was made to fit the LRS spectrum with amorphous carbon plus SiC. It is clear that neither model fits well. There may be SiC present in both circumstellar shells, but apparently the standard absorption coefficient, which is very successful in explaining most other observed features, does not work here. Note that in other stars which have comparably large optical depths (e.g. AFGL 865 [Fig. 16], AFGL 2494 [Fig. 38], or AFGL 2513 [Fig. 39]) a small fraction of SiC is required to obtain good fits to the LRS spectra.

6 THE TOTAL MASS-LOSS RATE AND DUST-TO-GAS RATIO

From the radiative transfer modelling the dust mass-loss rate has been derived. The values listed in Tab. 3 assume an opacity at 60 μm of 68 cm^{2}gr^{-1} and a dust velocity equal to the gas velocity. In this section the total mass-loss rate, the correction for the drift velocity and the dust-to-gas ratio are estimated.

The gas mass-loss rate can be derived, e.g. from CO observations. In a parallel study we have obtained new CO observations and their analyses will be presented in a separate paper. Here, the total mass-loss rate will be derived from equations similar to those in Netzer & Elitzur (1995) and Ivezić & Elitzur (1995), which are exact if radiation pressure is the force that drives the outflow (also see Appendix A1):

$$\dot{M} = 2.02 \times 10^{-8}\ \tau_{\rm F}\ \frac{L}{v_\infty - v_0}\ \left(1 - \frac{1}{\Gamma}\right) \qquad (M_\odot/yr) \qquad (5)$$

with $\tau_{\rm F}$ the flux-weighted optical depth at infinity, L the luminosity in solar units, v_∞ the terminal gas velocity, v_0 the gas velocity, in km s^{-1}, at the dust condensation radius, and Γ is the ratio of radiation pressure to gravitational pull. The mass loss rate can be derived when Γ is known. Its relation to physical quantities can be written down exactly (see Appendix A1), but is then in a form which is not suitable for practical calculations. In the Appendix an approximation is made which leads to the following form:

$$\Gamma = \frac{3\ Q_{\rm F}(\infty)\ L\ \Psi}{16\ \pi\ a\ \rho_{\rm d}\ c\ G\ M_\star}\ \frac{v_\infty}{v_\infty + v_{\rm drift}}, \qquad (6)$$

Table 4. Final results

IRAS-name	$\dot{M}^{(b)}$	$\dot{M}$	$\dot{M}$	$\Psi^{(c)}$	Ψ	Ψ	Ψ	Ψ	Γ	Γ	Γ	$v_{\rm dr}^{(d)}$	$v_{\rm dr}$	$v_{\rm dr}$	$v_{\rm dr}$	$v_{\rm dr}$
Model[(a)]	A,B,C	D	E	A	B	C	D	E	A,B,C	D	E	A	B	C	D	E
01144+6658	42.	41.	48.	1.3	1.2	0.59	1.3	1.2	10.8	8.3	10.5	1.3	0.4	1.9	1.3	1.2
02032+5636	–	–	–	–	–	–	–	–	–	–	–	–	–	–	–	–
02270−2619	2.0	1.7	2.2	0.20	0.15	0.10	0.23	0.19	2.5	2.1	2.4	8.2	2.6	12.2	8.8	7.7
02293+5749	27.	26.	32.	0.65	0.61	0.31	0.69	0.63	5.4	4.3	5.2	1.4	0.5	2.1	1.5	1.3
03229+4721	5.3	4.9	6.1	0.32	0.27	0.16	0.35	0.31	4.0	3.2	3.9	4.4	1.4	6.6	4.6	4.1
03243+4400	–	–	–	–	–	–	–	–	–	–	–	–	–	–	–	–
03488+3943	2.7	2.5	2.8	0.31	0.26	0.16	0.34	0.31	5.3	4.2	5.3	10.6	3.3	15.7	10.9	10.2
04562+0803	0.67	0.55	0.81	0.11	0.069	0.065	0.15	0.10	1.4	1.3	1.3	13.1	4.1	19.4	14.5	11.9
04573−1452	2.1	1.9	2.4	0.16	0.12	0.083	0.18	0.15	2.5	2.1	2.5	9.6	3.0	14.3	10.2	9.1
05185+3227	–	–	–	–	–	–	–	–	–	–	–	–	–	–	–	–
06012+0328	13.	12.	15.	1.1	1.0	0.53	1.2	1.1	8.7	6.8	8.5	2.2	0.7	3.2	2.2	2.0
06202+4743	0.18	0.16	0.20	0.24	0.14	0.14	0.29	0.23	2.3	2.0	2.2	35.0	11.1	51.9	37.4	33.2
06209+2503	0.10	0.077	0.13	0.23	0.11	0.15	0.35	0.21	1.1	1.1	1.1	26.8	8.5	39.8	31.0	23.9
06230−0930	5.6	5.1	6.4	0.31	0.27	0.15	0.34	0.30	3.2	2.7	3.2	4.0	1.3	6.0	4.2	3.8
06342+0328	10.	9.1	12.	0.27	0.24	0.13	0.30	0.26	3.2	2.6	3.1	2.8	0.9	4.2	3.0	2.6
06436+1840	–	–	–	–	–	–	–	–	–	–	–	–	–	–	–	–
06529+0626	1.8	1.6	1.9	0.20	0.16	0.11	0.23	0.20	3.9	3.1	3.8	13.3	4.2	19.7	13.9	12.8
07059+1006	–	–	–	–	–	–	–	–	–	–	–	–	–	–	–	–
07065−7256	3.2	2.9	3.6	0.23	0.19	0.12	0.26	0.22	3.1	2.5	3.0	6.9	2.2	10.3	7.3	6.6
07098−2012	6.0	5.8	6.6	0.64	0.56	0.32	0.67	0.63	9.8	7.6	9.7	5.6	1.8	8.4	5.7	5.4
07099+1441	–	–	–	–	–	–	–	–	–	–	–	–	–	–	–	–
08434−2801	0.33	0.30	0.43	0.40	0.22	0.24	0.45	0.34	3.5	2.9	3.3	17.2	5.4	25.5	18.0	15.0
09452+1330	11.	10.	13.	0.44	0.39	0.21	0.48	0.42	4.5	3.6	4.3	2.6	0.8	3.9	2.7	2.4
10324−5358	–	–	–	–	–	–	–	–	–	–	–	–	–	–	–	–
12447+0425	2.6	2.3	3.0	0.15	0.12	0.76	0.18	0.14	2.0	1.7	1.9	7.0	2.2	10.3	7.5	6.5
12536−5737	–	–	–	–	–	–	–	–	–	–	–	–	–	–	–	–
15194−5115	5.9	5.7	6.5	0.85	0.75	0.42	0.88	0.83	8.7	6.8	8.6	4.4	1.4	6.6	4.5	4.2
15477+3943	1.2	1.0	1.6	0.13	0.089	0.076	0.17	0.12	1.6	1.5	1.5	8.0	2.5	12.0	8.9	7.1
16239−1218	0.099	0.075	0.12	0.24	0.11	0.15	0.36	0.22	1.1	1.1	1.1	27.2	8.6	40.5	31.4	24.3
17556+5813	3.6	3.1	4.2	0.20	0.16	0.10	0.23	0.19	2.2	1.9	2.1	4.9	1.5	7.2	5.2	4.5
19008+0726	6.0	5.8	6.5	0.72	0.64	0.35	0.75	0.71	7.7	6.0	7.6	4.8	1.5	7.2	4.9	4.6
19175−0807	6.2	6.0	6.7	0.80	0.71	0.39	0.82	0.78	10.2	7.9	10.1	5.4	1.7	7.9	5.4	5.1
19321+2757	4.5	4.4	4.9	1.0	0.87	0.50	1.0	0.98	12.9	9.9	12.8	6.3	2.0	9.3	6.3	6.0
19594+4047	11.	11.	12.	1.1	0.97	0.51	1.1	1.0	11.2	8.6	11.0	3.2	1.0	4.7	3.2	3.0
20072+3116	7.3	7.0	7.9	0.90	0.82	0.43	0.95	0.89	7.7	6.0	7.6	3.8	1.2	5.7	3.9	3.7
20085−1425	2.1	1.7	2.5	0.16	0.12	0.086	0.20	0.15	1.7	1.5	1.6	5.9	1.9	8.7	6.4	5.3
20396+4757	3.9	3.5	4.6	0.20	0.17	0.10	0.23	0.19	2.1	1.8	2.1	4.5	1.4	6.7	4.8	4.2
20570+2714	6.2	6.1	6.8	1.1	0.93	0.52	1.1	1.0	14.3	11.0	14.2	5.4	1.7	8.0	5.4	5.1
21035+5136	5.9	5.1	7.1	0.18	0.15	0.093	0.21	0.17	2.3	2.0	2.2	3.7	1.2	5.5	3.9	3.3
21262+7000	2.7	2.3	3.1	0.15	0.12	0.077	0.18	0.14	1.8	1.6	1.7	6.1	1.9	9.0	6.6	5.6
21320+3850	4.3	3.9	5.0	0.25	0.21	0.13	0.28	0.24	3.0	2.5	2.9	4.7	1.5	6.9	4.9	4.3
22036+3315	0.48	0.42	0.57	0.14	0.083	0.084	0.17	0.13	2.0	1.8	2.0	20.0	6.3	29.7	21.5	18.4
23166+1655	16.	15.	19.	2.0	1.9	0.97	2.1	2.0	11.4	8.8	11.0	1.6	0.5	2.3	1.6	1.4
23320+4316	9.4	8.8	11.	0.54	0.48	0.26	0.58	0.52	5.1	4.1	5.0	2.7	0.9	4.1	2.8	2.5

(a). Model A is the standard model with $a = 0.1$ μm, $\kappa_{60} = 68$ cm^{2}g^{-1}, $M_\star = 0.6$ M$_\odot$ and $v_0 = 1$ km s^{-1}. Model B has $a = 0.01$ μm, Model C has $\kappa_{60} = 150$ cm^{2}g^{-1}, Model D has $M_\star = 0.8$ M$_\odot$ and Model E has $v_0 = 3$ km s^{-1}. All other parameters are unchanged with respect to Model A.
(b). Mass loss rates are in units of 10^{-6} M$_\odot$yr^{-1}.
(c). Dust-to-gas ratios are in units of 0.01.
(d). Drift velocities in km s^{-1}.

where c is the speed of light, G the gravitational constant and $M_\star$ the mass of the star; the other symbols have been defined previously. This approximation should yield accurate results when Γ is large, so its precise value does not influence the derivation of the mass loss rate. For small values of Γ the accurateness may be less but should still give more realistic results than assuming that Γ is large.

We also define a quantity y_0 as follows:

$$y_0 \equiv 1 - \left(\frac{v_0^2}{v_\infty^2 - v_0^2} \right) \tag{7}$$

and

$$Y \equiv 2 \left(1 - \sqrt{1 - y_0}\right) / y_0. \tag{8}$$

The derivation of the mass-loss rate and and dust-to-gas ratio then proceeds as follows:

(i) Choose values for the grain size (a), the opacity at 60 μm (κ), the mass of the star ($M_\star$) and the gas velocity (v_0) at the condensation point. Calculate the effective absorption coefficient by multiplying the value in Tab. 3 by ($a/0.1 \times \kappa/68$), and the dust mass-loss rate by multiplying the value in Tab. 3 by ($\kappa/68$), and divide by Y (Eq. 8) to get the first order correction for the effect of the dust velocity law (this is explained in Appendix A1). Initially set Γ to a large value.
(ii) Calculate the mass-loss rate using Eq. (5) with the values of L, v_∞ and $\tau_{\rm F}$ from Tabs. 2 and 3.
(iii) Calculate the drift velocity ($v_{\rm drift}$) from Eq. (2).
(iv) Calculate the dust mass-loss rate, by multiplying the value found under step (i) by $(v_\infty + v_{\rm drift})/v_\infty$, and then the resulting dust-to-gas ratio (Ψ).
(v) Calculate Γ from Eq. (6).
(vi) Go to step (ii), and iterate until the value of Γ has converged.

This procedure can be followed for all stars, except those without detected gas expansion velocity, and those for which no dust mass-loss rate could be derived.

Models have been run using this procedure for five different sets of parameters. Model A, with the default parameters $a = 0.1$ μm, $\kappa_{60} = 68$ cm^{2}g^{-1}, $M_\star = 0.6$ M$_\odot$, $v_0 =$ 1 km s^{-1}, and models with $a = 0.01$ μm (Model B), $\kappa_{60} =$ 150 cm^{2}g^{-1} (Model C), $M_\star = 0.8$ M$_\odot$ (Model D) and v_0 = 3 km s^{-1} (Model E). The results are collected in Tab. 4, where the mass-loss rate, the dust-to-gas ratio, Γ and the drift velocity are listed.

The effect of lowering the grain size is primarily to lower Q, as Q/a is approximately constant. This reduces the drift velocity. The dust mass-loss rate, and hence Ψ, change slightly due to the different drift velocity. Γ remains constant however, as the same term with the drift velocity ($v_\infty + v_{\rm drift}$) appears in Eq. (6). The effect of increasing κ_{60} is first of all to increase Q. This leads to higher drift velocities. A second effect is that the dust mass-loss rate (even apart from the change in the drift velocity) must decrease, to keep the optical depth constant (Eq. 1). Γ remains constant, as the direct effect of the change in Q and Ψ cancel, as well as the secondary effect due to the change in $v_{\rm drift}$. The effect of increasing $M_\star$ is to lower Γ, which lowers the mass-loss rate, which changes the drift velocity and Ψ. The effect of increasing v_0 is to increase the mass-loss rate, which in turn affects all other parameters.

7 DISCUSSION

7.1 Mass-loss rate and dust-to-gas ratio

In Fig. 1 the mass-loss rates and dust-to-gas ratios as derived from Model A in Tab. 4 are plotted against pulsation period and luminosity (the filled squares). There is a good correlation between log $\dot{M}$ and log L and log P over the entire range. Least-squares fitting on the 36 data points give the following results:

$$\log \dot{M} = (4.08 \pm 0.41)\ \log P - (16.54 \pm 1.10);\ \sigma = 0.27, \quad (9)$$

and

$$\log \dot{M} = (3.94 \pm 0.28)\ \log L - (20.79 \pm 1.10);\ \sigma = 0.28. \quad (10)$$

The results for models B–E are insignificantly different. As we assumed a $P - L$-relation from the start, these relations are not independent. If we had assumed a constant luminosity for all stars, we still would have found a significant relation between mass loss rate and pulsation period.

Whitelock (1990, 1994) derived the mass-loss rates for oxygen-rich Miras in the Galactic Bulge and at high galactic latitude, respectively. The dashed polygon in Fig. 1 indicates the region wherein most of the former sample is located while the dotted polygon indicates the region wherein most of the later sample is located.

The relations for oxygen-rich and carbon Miras appear to be similar. There are some caveats however. The mass-loss rates for the oxygen-rich Miras were not derived from model fits to the SEDs, but from Jura's (1987) formula which relates mass-loss rate to the IRAS flux, luminosity, mean wavelength of the emergent light, dust-to-gas ratio and expansion velocity. Whitelock assumed a constant dust-to-gas ratio and a constant expansion velocity for all of the stars in a given sample. As we show below, the dust-to-gas ratio for carbon stars appears to be a function of period, and there is a large spread in expansion velocity at a given period. If the same holds for oxygen-rich stars then there will be systematic uncertainties in the derived mass-loss rates of the two samples of O-rich Miras.

The dust-to-gas ratio appears to be rather constant at a value of 0.0025 up to $P \approx 500$ days, or $L \approx 7900$ L$_\odot$, and then increase markedly to values up to 0.015. AFGL 3068 appears to have an extremely high dust-to-gas ratio of about 0.02. The absolute values of the derived ratio depend somewhat on the model (see Table 4) but the trend remains the same.

Figure 2 shows the relation between the mass-loss rate and the amplitude of variability in the K-band. As is well known, larger amplitude implies larger mass-loss rate. A least-squares fit, excluding the open symbols which represent the stars for which no mass-loss rate could be derived, and the two stars at $\dot{M} \approx 10^{-7}$ M$_\odot$ yr^{-1}, is:

$$\log \dot{M} = (0.62 \pm 0.07)\ \Delta K - (6.12 \pm 0.10);\ \sigma = 0.14. \quad (11)$$

A similar plot for oxygen-rich Miras was shown by Whitelock (1990, 1994) for the samples of oxygen-rich stars discussed above. The dashed polygon indicates the region within which most of the Galactic Bulge stars are located, and the dotted polygon the region within which most of the high-latitude Miras are located. There is considerable overlap between these regions.

For some stars, and some models, the drift velocities are larger then 20 km s^{-1}. This is the approximate limit where sputtering is thought to destroy dust grains (Salpeter 1977), although Krüger & Sedlmayr (1996) put the limit at 40 km s^{-1}. As can be seen from Tab. 4, and as discussed above, smaller grains than the default value of 0.1 μm make the drift velocity smaller. This has no influence on the mass-loss rate, and a small effect on the dust-to-gas ratios.

7.2 Expansion velocity

Figure 3 shows the observed expansion velocity plotted luminosity and pulsation period. The other correlations are poor. A similar result was found by Wood (1990) for O-rich Miras, although he nevertheless had the courage to fit a straight line through his data points: the dotted line in Fig. 3. Lepine et al. (1995) found a relative good correlation for OH/IR stars up to 700 days, which is the dashed line in Fig. 3.

In order to make a more general comparison between oxygen-rich and carbon-rich Miras, we selected from the literature data on the CO and/or OH expansion velocities of O-rich Miras and OH/IR stars with known periods. More details on the selection procedure can be found in Appendix A2. The results are plotted as the dots in the bottom panel of Fig. 3.

There is a good deal of overlap between the regions occupied by O-rich and C-rich stars, although for periods below 600 days the carbon stars appear to lie systematically above the oxygen-rich Miras. For large periods the expansion velocities seem to level off. For both oxygen- and carbon-rich stars there is a scatter of up to a factor of 2 in velocity at a given period.

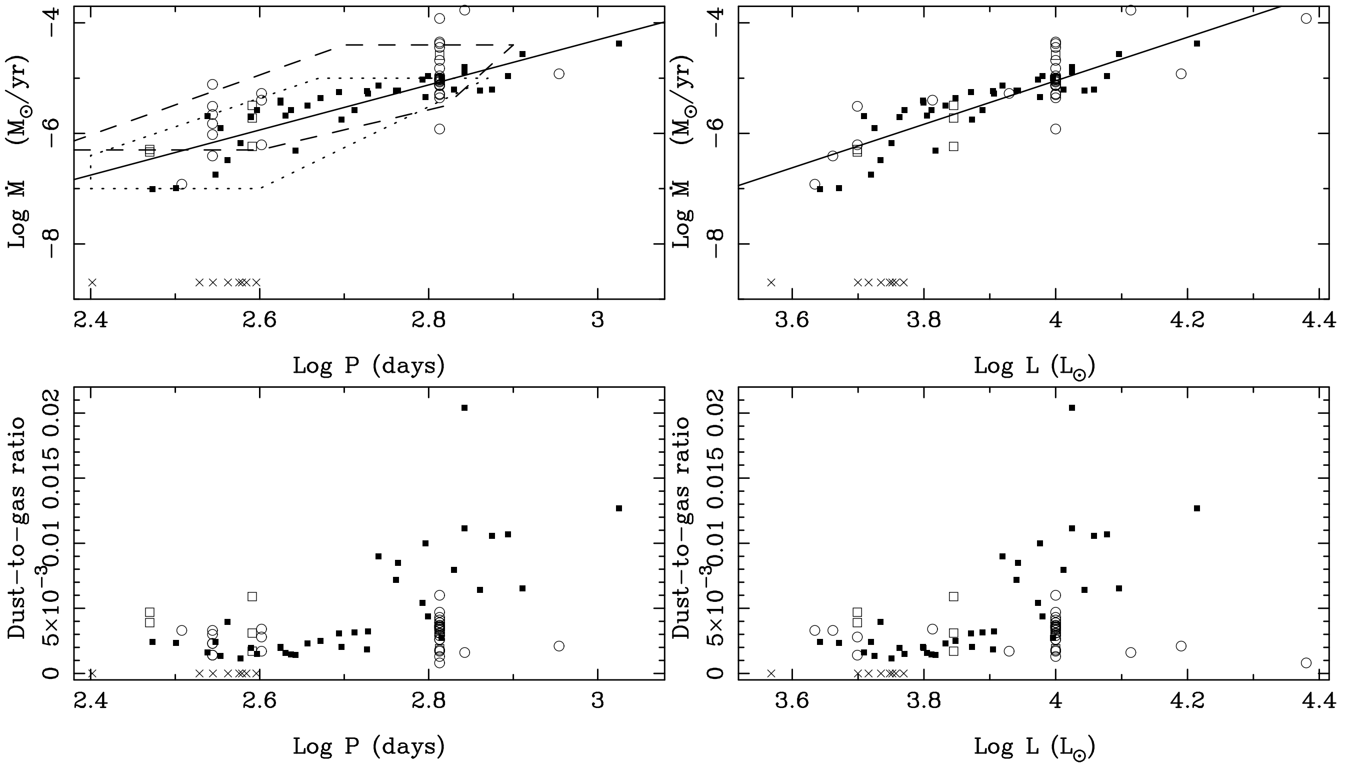

Figure 1. Mass-loss rate and dust-to-gas ratio, according to Model A in Tab. 4, versus pulsation period and luminosity (filled squares). The crosses plotted at a mass-loss rate of 2 10^{-9} $M_\odot\,yr^{-1}$ and $\Psi = 0$ are stars without measured expansion velocity or for which no dust mass-loss rate could be derived. The solid lines are least-squares fits (see Eqs. 9-10). The dashed and dotted polygons indicate regions occupied by different samples of oxygen-rich Miras (see text). The open squares and circles represent selected models from radiation-hydrodynamical calculations including dust formation from the Vienna and Berlin groups, respectively (see text).

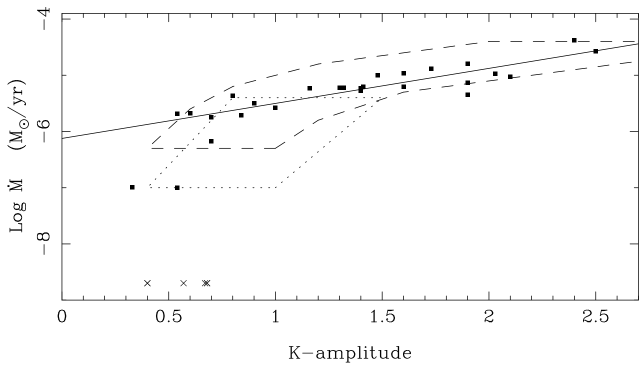

Figure 2. Mass-loss rate according to Model A in Tab. 4, versus amplitude in the K-band. The crosses plotted at a mass-loss rate of 2 10^{-9} $M_\odot\,yr^{-1}$ are stars for which no dust mass-loss rate could be derived. The solid line is a least-squares fit (see Eq. 11). The dashed and dotted polygons represent the area where oxygen-rich stars in the galactic bulge and at high galactic latitude are located (see text).

7.3 Comparison with theoretical models

Two groups (Berlin and Vienna) calculate radiation-hydrodynamical models of the atmospheres and circumstellar shells of carbon-rich long-period variables which include dust formation (see Höfner et al. 1996 for details and a comparison between the two groups). In this section we compare selected models with our derived parameters.

From the Vienna group we take the models of Höfner & Dorfi (1997). As pulsation period and luminosity are independent variables in these models, some combinations they calculate are not in agreement with the period-luminosity relation we use in this paper. Therefore we restrict ourselves to the following models (in their notation): P1, P2, P4, P5 (650 days, 10000 $L_\odot$), R5, R5C (295 days, 5000 $L_\odot$), R7, R7C20, R7C18 (390 days, 7000 $L_\odot$). In all cases the stellar mass is 1 $M_\odot$ in these models. The differences between the models of a given period and luminosity are the C/O ratio (for the 295 and 390 day models) and/or the effective temperature.

From the Berlin group we take the following models from Fleischer et al. (1992) and Arndt et al. (1997), again only those with luminosities in accordance with our adopted $P-L$ relation. In their notation: from Fleischer et al. models A (350 days, 4590 $L_\odot$), B (322 days, 4310 $L_\odot$), C (400 days, 6500 $L_\odot$), E (650 days, 10 000 $L_\odot$), F (900 days, 15 500 $L_\odot$); from Arndt et al. models 2, 4, 9, 13-19, 22-24, 26-29 (all these 17 model with 650 days, 10 000 $L_\odot$), 34 (350 days, 5000 $L_\odot$), 35 (400 days, 8500 $L_\odot$), 36-37 (650 days, 10 000 $L_\odot$), 40 (400 days, 5000 $L_\odot$), 41-43 (350 days, 5000 $L_\odot$), 44 (350 days, 5500 $L_\odot$), 47 (650 days, 10 000 $L_\odot$). Again, the differences between models with the same period and luminosity is in stellar mass, effective temperature, C/O ratio and/or piston velocity amplitude. Additionally we take the models specifically designed to fit IRC +10 216 (Winters et al. 1997; 650 days, 24 000 $L_\odot$), which is a combination of P and L that does not fit our $P-L$ relation, and AFGL 3068 (Fleischer et al. 1997; 696 days, 13 000 $L_\odot$). Note that the models were not all calculated with exactly the same physics (see Arndt et al. 1997 for details).

All of the models provide mass-loss rates, time averaged dust-to-gas ratios and expansion velocities. The model results are plotted as the open squares (Vienna models) and open circles (Berlin models) in Figs. 1 and 3.

In general, the mass-loss rates these models predict are in good agreement with observed values derived in the present paper (Fig. 1). The exception being the models specifically designed to fit IRC +10 216 (Winters et al. 1997) and AFGL 3068 (Fleischer et al. 1997). Apart from having a luminosity inconsistent with the $P-L$ relation, their proposed mass-loss rate of 1.2×10^{-4} $M_\odot$ yr^{-1} for IRC +10 216 is larger than the upper limit of 4×10^{-5} $M_\odot$ yr^{-1} derived by Keady & Ridgway (1993) from the non-detection of the H_2 S(1) rotation line at 17.0 μm. We find a mass-loss rate of 1.1-1.3 $\times 10^{-5}$ $M_\odot$ yr^{-1}.

Regarding the dust-to-gas ratio there is good agreement for short periods and low luminosities, in particular if one considers that there may be systematic uncertainties due to the uncertainty in the absolute values of the dust opacity. For longer periods and higher luminosity there is a systematic difference in the sense that the theoretical models predict similar, and observations suggest higher, dust-to-gas ratios than at shorter periods.

Regarding the expansion velocities (Fig. 3) one notices that the theoretical models predict velocities for short period/low luminosity Miras which are too large compared to observations. This could be partly because the theoretical models neglect the drift velocity and thus predict the dust velocity, while the velocity which is observed is that of the gas. On the other hand it is also clear that the C/O ratio predominantly determines the final velocity in the theoretical models. This is nicely demonstrated by the three Vienna models at 7000 $L_\odot$, or 390 days. As the C/O ratio goes up from 1.8 to 2.0 to 2.5, the expansion velocity goes up from 7 to 21 to 33 km s^{-1}, with all other parameters remaining the same. The observations suggest therefore a C/O ratio between 1.8 and 2.0 for stars of these luminosities. The two Berlin models at 5000 $L_\odot$ (Periods of 350 and 400 days) are in good agreement with the observations. They are calculated with C/O ratios of 1.50 and 1.60. At the shortest periods, the two Vienna models are calculated with C/O ratios of 2.30 and 2.50. The observations therefore imply C/O ratios smaller than about 2. At the lowest luminosities the four Berlin models are calculated with C/O ratios of 1.50 and 1.70. Again, the observations imply C/O ratios smaller than this. This is consistent with the C/O ratios determined in 30 carbon-rich semi-regular and irregular variables with little or no dust by Lambert et al. (1986) who find that the largest C/O ratio is 1.6, and 50% of the stars in their sample have C/O < 1.1. An increase of the C/O ratio with luminosity is also consistent with an evolutionary picture in which stars with higher luminosity evolve from stars of higher initial mass; these have experienced more thermal pulses and thus dredged-up more carbon (see the scenario by Groenewegen et al. 1995).

The reason why the Berlin and Vienna groups calculate models with low luminosity only for large C/O ratios is that

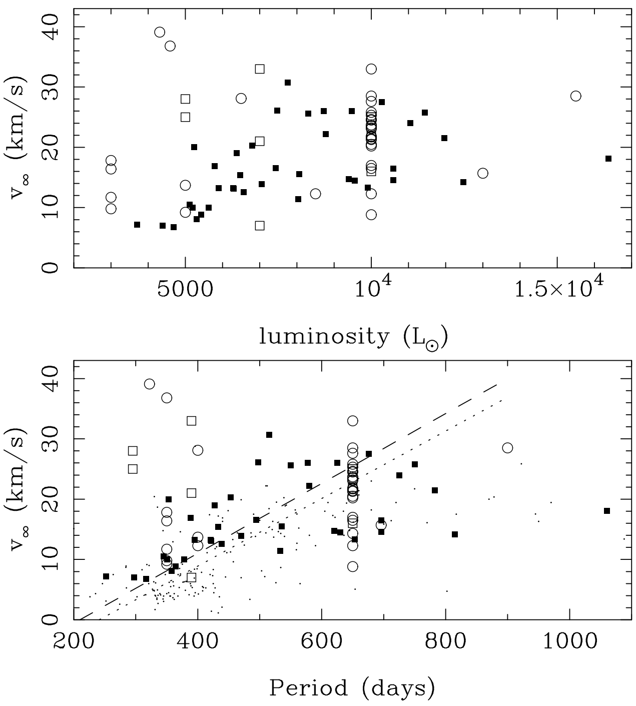

Figure 3. Observed expansion velocity plotted versus luminosity and pulsation period. The dashed and dotted lines are expressions in the literature for oxygen-rich stars (see text). The open squares and circles represent radiation-hydrodynamical model calculations (see text). The dots represent observed values of expansion velocities based on CO or OH observations for O-rich Miras and OH/IR stars (see text).

only under these conditions do their models predict outflows. This reveals a limitation of the current state of modelling. It could imply there is an additional outward directed force besides radiation pressure on dust, possibly radiation pressure on molecules (Jørgensen & Johnson 1992), acoustic waves (Pijpers & Habing 1989), or Alfvén waves (Hartmann & MacGregor 1980). Alternatively, the flow may not be homogeneous, but clumpy, which could lead to localised dust formation. Clumpy structures are seen in the CO emission around the carbon stars with detached shells (e.g. Bergman et al. 1993, Olofsson et al. 1996).

7.4 Colour versus optical depth

The procedure outlined in Sect. 6 to obtain the mass-loss rate and dust-to-gas ratio, under the assumption that mass loss is driven by radiation pressure on dust, requires knowledge of the flux-weighted optical depth, τ_F. Unless one does the radiative transfer modelling this quantity is unknown. Ivezić & Elitzur (1995) proposed a calibration of τ_F against $(\nu F_\nu)_{60}/F$, not only for carbon-rich dust, but also for silicate dust. In Fig. 4 τ_F is plotted against $(\nu F_\nu)_{60}/F$, $J-K$, $K-L'$ and $12-25$ colour. The relation suggested by Ivezić & Elitzur (1995) is represented by the solid line. Our results differ significantly from their best fit. The reason is not immediately obvious. One reason for the discrepancy is that their line is intended to fit not only their results for a grain mixture of SiC and AMC (in a fixed ratio of 1:4),

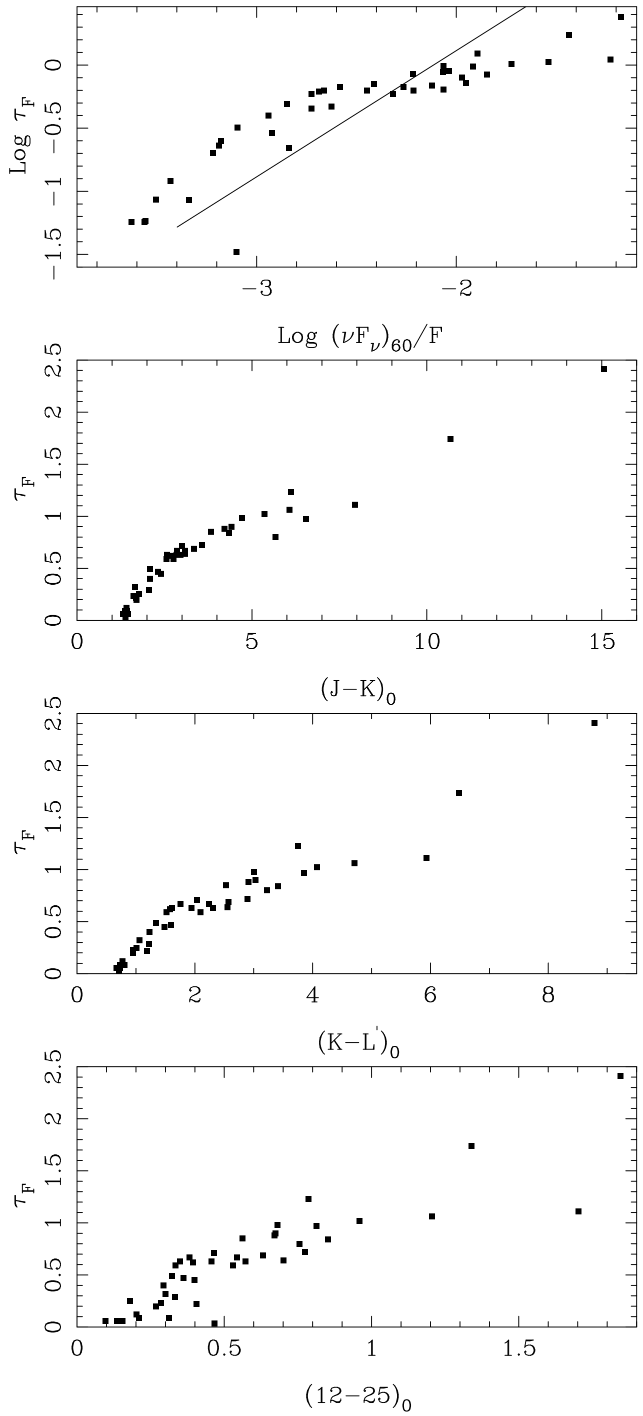

Figure 4. The flux-weighted optical depth versus $(\nu F_\nu)_{60}/F$, $J-K$, $K-L'$ and $12-25$ synthetic colours (dereddened). The solid line in the upper panel is the relation suggested by Ivezić & Elitzur (1995).

but also silicates + AMC, Olivine + silicates, and pure silicates and AMC. Their result for a mixture of SiC + AMC lies above the general fit and is also curved, similar to our result. Nevertheless the differences in Fig. 4 are larger than can be accounted for by this effect alone.

7.5 Colour versus Period relations

In a recent paper, Lepine et al. (1995) discussed some relations between colours and pulsation period and/or luminosity for OH/IR stars. Here we attempt to extend this to a larger sample of O-rich stars and make a comparison with the carbon star sample.

In order to circumvent the effect of variability, and the different photometric systems on which the infrared data were taken, we did not take the original observational data, but instead convolved our final model fits of the carbon stars with the ESO $JHKL'M$, and IRAS photometric filter response curves, and applied the appropriate zero points, to obtain unreddened synthetic colours (see Groenewegen 1997b).

For the oxygen-rich stars this is not possible, and therefore the observed colours are shown without reddening correction. The sample selection of the O-rich Miras and OH/IR stars is discussed in Appendix A2. It is important to note that only photometry on the ESO system is plotted.

In Fig. 5 the synthetic colours of the carbon stars (open squares), and the observed colours for the O-rich Miras and OH/IR stars (dots) are plotted against pulsation period (bottom 3 panels); these are all on the IRAS and ESO systems. There is a clear trend that redder colours are associated with longer periods. In fact, for periods longer than 450 days one may make a rough estimate of the period from the colours, if a given carbon star is thought to be a Mira variable, but its period has not been determined. This could be particularly useful in statistical studies when large sets of infrared photometry are available of stars (e.g. the upcoming large scale DENIS and 2MASS infrared surveys), for which no periods will generally be available.

The oxygen-rich and carbon stars behave similarly in the $J-K$ and $K-L'$ colour plots, but there is a significant offset in the $12-25$ colour. This is due to the strong silicate emission feature in O-rich stars with optically thin shells. In the top panel of Fig. 5 the $12-25$ versus $K-L'$ colour-colour plot is shown (e.g. Epchtein et al. 1987). As shown in that paper, and confirmed here, O- and C-stars separate nicely in this colour-colour diagram. In practice this means that in statistical studies one can use the $12-25$ versus $K-L'$, or similar colour-colour plots to distinguish carbon from oxygen-rich stars, and then use the colour versus period plots to infer the period. One could then use a $P-L$-relation to obtain the luminosity, and thus derive a distance estimate from the observed flux and a suitable bolometric correction (e.g. Groenewegen 1997b).

Acknowledgements

This research has made use of the SIMBAD database, operated at CDS, Strasbourg, France. The 1994 observing trip of M.G. to the Anglo-Australian Telescope and his subsequent stay at ADFA were made possible by financial support from the Franco-Australian fund for scientific collaboration. Suzanne Ramsay & Tom Geballe are thanked for taking the UKIRT CGS3 spectra. The United Kingdom Infrared Telescope is operated by the Joint Astronomy Centre on behalf of the U.K. Particle Physics and Astronomy Research Council. Josef Wagenhuber is thanked for critically reading Appendix A1. An anonymous referee made criti-

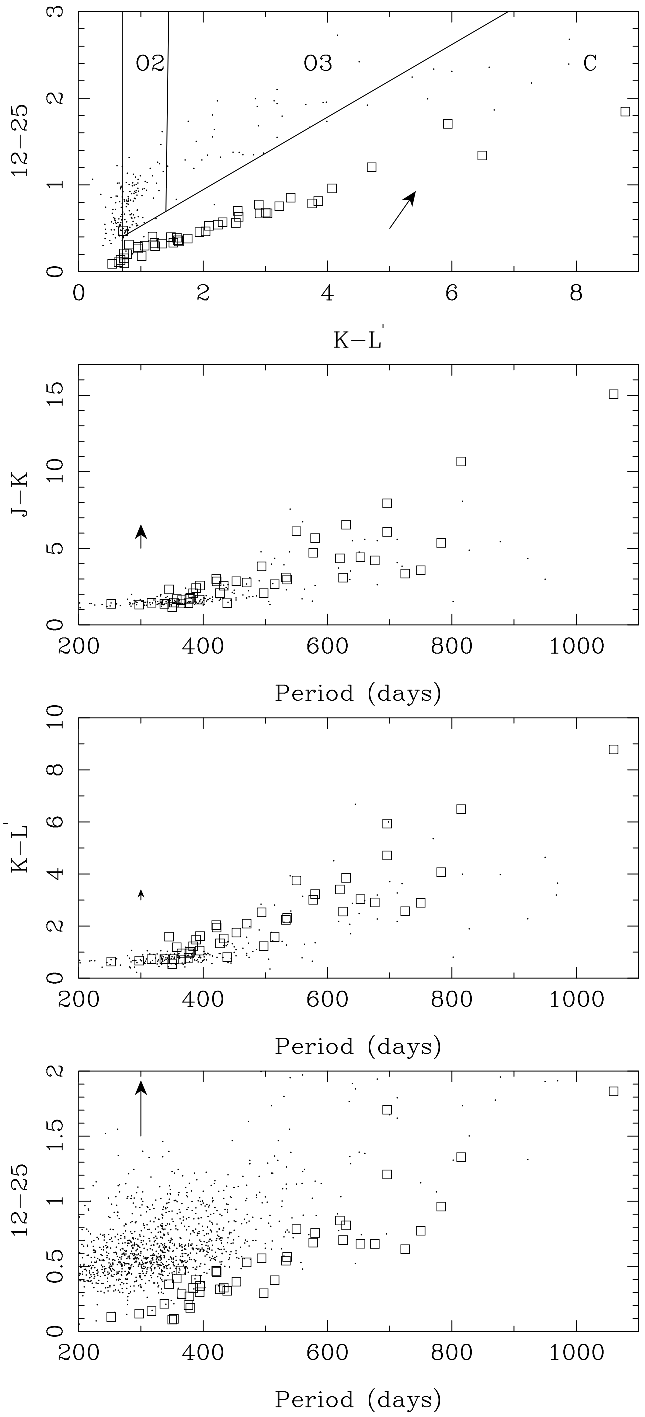

Figure 5. $[K-L']$ versus $[12-25]$ colour-colour diagram, and $[J-K]$, $[K-L']$ and $[12-25]$ colour versus pulsation period. The open squares represent the carbon Miras from the present sample, with dereddened synthetic colours. The dots represent observations of known O-rich Miras and OH/IR stars (see text). The segments marked 'O2', 'O3', 'C' indicate regions predominantly occupied by O-stars and C-stars, respectively (see Epchtein et al. 1987). The arrows mark the shift in colour when corrected for a $A_{\rm V}$ of 10 magnitudes.

cal remarks which improved the presentation. Jacques Lepine and Robero Ortiz are thanked for making their database on OH/IR stars available in computer readable form. This work is supported by the *Fonds zur Förderung der wissenschaftlichen Forschung* under project number S7308-AST. We also thank Freddy Marang, Michael Feast and Brian Carter for making some of the infrared observations in Table 1.

REFERENCES

Alknis A., 1980, Investigations of the sun and red stars 11, 5
Altenhoff W.J., Thum C., Wendker H.J., 1994, A&A 281, 161
Aitken D.A., Roche P.F., 1982, MNRAS 200, 217
Arndt T.U., Fleischer A.J., Sedlmayr E., 1997, A&A, in press
Bagnulo S., Doyle J.G., Griffin I.P., 1995, A&A 301, 501
Barnes T.G., 1973, ApJS 25, 369
Bedijn P.J., 1987, A&A 186, 136
Bergeat J., Sibille F., Lunel M., Jefevre J., 1976, A&A 52, 227
Bergeat J., Lunel M., 1980, A&A 87, 139
Bergman P., Carlström U., Olofsson H., 1993, A&A 268, 685
Burstein D., Heiles C., 1982, AJ 87, 1165
Cardelli J.A., Clayton G.C., Mathis J.S., 1989, ApJ 345, 245
Carter B.S., MNRAS 242, 1
Catchpole R.M., Robertson B.S.C., Lloyd Evans T.H.H., Feast M.W., Glass I.S., Carter B.S., 1979, SAAO Circ. 1, 61
Celis S.L., 1982, AJ 87, 1791
Chan S.J., Kwok S., 1990, A&A 237, 354
Chapman J.M., Habing H.J., Killeen N.E.B., 1995, in: "Astrophysical applications of stellar pulsation", ASP conf. ser. 83, Eds. R.S Stobie and P.A. Whitelock, p. 113
Cohen M., 1984, MNRAS 206, 137
Cohen M., Kuhi L.V., 1977, PASP 89, 829
Cohen M., Walker R.G., Witteborn F.C., 1992, AJ 104, 2030
Danchi W.C., Bester M., Degiacomi C.G., Greenhill L.J., Townes C.H., 1994, AJ 107, 1469
Dyck H.M., Lockwood G.W., Capps R.W., 1974, ApJ 189, 89
Eggen O.J., 1975, ApJS 29, 77
Engels D., Kreysa E., Schultz G.V., Sherwood W.A., 1983, A&A 124, 123
Engels D., Schultz G.V., Sherwood W.A., 1981, in: "Physical processes in red giants", Eds. I. Iben and A. Renzini, Reidel, Dordrecht, p. 401
Epchtein N., et al., 1987, A&AS 71, 39
Epchtein N., Le Bertre T., Lépine J.R.D., 1990, A&A 227, 82
Fleischer A.J., Gauger A., Sedlmayr E., 1992, A&A 266, 321
Fleischer A.J., Winters J.-M., Le Bertre T., Sedlmayr E., 1997, in: "The impact of large scale near-infrared surveys", Ed. F. Garzón et al., p. 101
Forrest W.J., Gillett F.C., Stein W.A., 1975, ApJ 195, 423
Fouqué P., Le Bertre T., Epchtein N., Guglielmo F., Kerschbaum F., 1992, A&AS 93, 151
Gail H.-P., Sedlmayr E., 1986, A&A 161, 201
Gaylard M.J., West M.E., 1995, in: "Astrophysical applications of stellar pulsation", ASP conf. ser. 83, Eds. R.S Stobie and P.A. Whitelock, p. 113
Gehrz R.D., Hackwell J.A., 1976, ApJ 206, L161
Gehrz R.D., Ney E.P., Grasdalen G.L., Hackwell J.A., Thronson H.A., 1984, ApJ 281, 303
Gillett F.C., Merrill K.M., Stein W.A., 1971, ApJ 164, 83
Gosnell T.R., Hudson H., Puetter R.C., 1979, AJ 84, 538
Grasdalen G.L., Gehrz R.D., Hackwell J.A., Castelaz M., Gullixson C., 1983, ApJS 53, 413
Griffin I.P., 1990, MNRAS 247, 591
Griffin I.P., 1993, MNRAS 260, 831

Groenewegen M.A.T., 1993, Chapter 5, Ph.D. thesis, University of Amsterdam
Groenewegen M.A.T., 1995a, A&A 293, 463 (G95)
Groenewegen M.A.T., 1995b, in: "Circumstellar matter", eds. G.D. Watt & P.M. Williams, Kluwer, Dordrecht, p. 321
Groenewegen M.A.T., 1995c, in: "Astrophysical applications of stellar pulsation", eds. R.S. Stobie and P.A. Whitelock, ASP conf. series 83, p. 141
Groenewegen M.A.T., 1997a, A&A 317, 503
Groenewegen M.A.T., 1997b, in: "The impact of large-scale infrared surveys", eds. F. Garzón et al., p. 165
Groenewegen M.A.T., Baas F., de Jong T, Loup C., 1996a, A&A 306, 241
Groenewegen M.A.T., Baas F., Blommaert J.A.D.L., Josselin E., Tilanus R.P.J., 1996b, in: "Science with large millimetre arrays", ed. P. Shaver, ESO, p. 286
Groenewegen M.A.T., de Jong T., 1993, A&AS 101, 267
Groenewegen M.A.T., de Jong T., 1994, A&A 281, 115
Groenewegen M.A.T., de Jong T., Baas F., 1993, A&AS 101, 513
Groenewegen M.A.T., de Jong T., Geballe T.R., 1994, A&A 287, 163
Groenewegen M.A.T., de Jong T., van der Bliek N.S., Slijkhuis S., Willems F.J., 1992, A&A 253, 150
Groenewegen M.A.T., van den Hoek L.B., de Jong T., 1995, A&A 293, 381
Groenewegen M.A.T., van Loon J. TH., Whitelock P.A., Wood P.R., Zijlstra A.A., 1997, in: "IAU symposium 177: The carbon star phenomenon", eds. TBD, p. TBD
Groenewegen M.A.T., Whitelock P.A., 1996, MNRAS 281, 1347
Guglielmo F., et al., 1993, A&AS 99, 31
Habing H.J., Tignon J., Tielens A.G.G.M., 1994, A&A 286, 523
Hackwell J.A., 1972, A&A 21, 239
Hartmann L, MacGregor K.B., 1980, ApJ 242, 260
Höfner S., Dorfi E.A., 1997, A&A 319, 648
Höfner S., Fleischer A.J., Gauger A., Feuchtinger M.U., Dorfi E.A., Winters J.M., Sedlmayr E., 1996, A&A 314, 204
Ivezić Z., Elitzur M., 1995, ApJ 445, 415
Ivezić Z., Elitzur M., 1996, MNRAS 279, 1011
Jiménez-Esteban F.M., Garcia-Lario P., Manchado A., Engels D., 1997, in: "The impact of large scale near infrared surveys", Eds. F. Garzón et al., p. 103
Joint IRAS Science Working Group, 1986, IRAS catalogs and atlases, Low Resolution Spectrograph (LRS), A&AS 65, 607
Joint IRAS Science Working Group, 1986, IRAS catalogs and atlases, Point Source Catalog (PSC), US Government Printing Office, Washington
Joint IRAS Science Working Group, 1986, IRAS catalogs and atlases, Explanatory Supplement, US Government Printing Office, Washington
Jones B., Merrill K. M., Puetter R. C., Willner S. P., 1978, AJ 83, 1437
Jones T.J., et al., 1990, ApJS 74, 785
Jørgensen U.G., Johnson H.R., 1992, A&A 265, 168
Jørgensen U.G., Westerlund B.E., 1988, A&AS 72, 193
Joyce R.R., Merrill K.C., Gillett F.C., 1997, in preparation
Jura M., 1984, ApJ 286, 630
Jura M., 1986, ApJ 303, 327
Jura M., 1987, ApJ 313, 743
Justtanont K., Barlow M.J., Skinner C.J., Roche P.F., Aitken D.K., Smith C.H., 1996, A&A 309, 612
Justtanont K., Tielens, A.G.G.M., 1992, ApJ 389, 400
Keady J.J., Ridgway S.T., 1993, ApJ 406, 199
Kholopov P.N., et al., 1985, General Catalog of Variable Stars (GCVS), Nauka, Moscow
Krüger D., Sedlmayr E., 1996, A&A, in press
Kwan J., Hill F., 1977, ApJ 215, 781
Lambert D.L., Gustafsson B., Eriksson K., Hinkle K., 1986, ApJS 62, 373
Landolt U., 1968, PASP 80, 680
Landolt U., 1969a, AJ 81, 134
Landolt U., 1969b, AJ 81, 381
Landolt U., 1973, PASP 85, 625
Lázaro C., et al., 1994, MNRAS 269, 365
Le Bertre T., 1987, A&A 176, 107
Le Bertre T., 1988a, A&A 190, 79
Le Bertre T., 1988b, A&A 203, 85
Le Bertre T., 1992, A&AS 94, 377
Le Bertre T., 1993, A&AS 97, 729
Lebofsky M.J., Rieke G.H., 1977, AJ 82, 646
Lebofsky M.J., Sargent D.G., Kleinmann S.G., Rieke G.H., 1978, ApJ 219, 487
Lepine J.R.D., Ortiz R., Epchtein N., 1995, A&A 299, 453
Lequeux J., Jourdain de Muizon M., 1990, A&A 240, L19
Le Sidaner P., Le Bertre T., 1993, A&A 278, 167
Le Squeren A.M., Sivagnanam P., Dennefeld M., David P., 1992, A&A 254, 133
Lockwood G.W., 1972, ApJS 24, 375
Lockwood G.W., 1974, ApJ 192, 113
Lockwood G.W., 1985, ApJS 58, 167
Lopez B., Perrier C., Mékarnia D., Lefèvre J, Gay J., 1993, A&A 270, 462
Lorenz-Martins S., Lefèvre J., 1993, A&A 280, 567
Lorenz-Martins S., Lefèvre J., 1994, A&A 291, 831
Lorenz-Martins S., 1996, A&A 314, 209
Loup C., Forveille T., Omont A., Paul J.F., 1993, A&AS 99, 231
Low F.J., Kurtz R.F., Vrba F.J., Rieke G.H., 1976, ApJ 206, L153
Martin P.G., Rogers C., 1987, ApJ 322, 374
Meadows P.J., Good A.R., Wolstencroft R.D., 1987, MNRAS 225, 43P
Merrill K.M., Stein W., 1976, PASP 88, 294
Mitchell R.M., Robinson G., 1980, MNRAS 190, 669
Munari U., Yudin B.F., Taranova O.G., Massone G., Marang F., Roberts G., Winkler H., Whitelock P.A., 1992, A&AS 93, 383
Neckel Th., Klare G., 1980, A&AS 42, 251
Netzer N., Elitzur M., 1993, ApJ 410, 701
Neugebauer G., Leighton R.B., 1969, NASA SP-3047
Ney E.P., Merrill K.M., 1980, AFGL-TR-80-0050
Nicolet B., 1978, A&AS 34, 1
Noguchi K., et al., 1981, PASJ 33, 373
Nyman L.-A., Hall P.J., Le Bertre T., 1993a, A&A 280, 551
Nyman L.-A., Olofsson H., Johansson L.E.B., Booth R.S., Carlstrom U., Wolstencroft R., 1993b, A&A 269, 377
Olofsson H., Bergman P., Eriksson K., Gustafsson B., 1996, A&A 311, 587
Olson B.I., Richer H.B., 1975, ApJ 200, 88
Omont A., et al., 1996, private communication
Orofino V., Colangeli L., Bussoletti E., Blanco A., Fonti S., 1990, A&A 231, 105
Ortiz R., Maciel W.J., 1996, A&A 313, 180
Parenago P.P., 1940, Astron. Zh. 17, 3
Pégourié B., 1988, A&A 194, 335
Pijpers F.P., Habing H.J., 1989 A&A 215, 334
Price S.D., Murdock T.L., 1983, The revised AFGL infrared sky survey catalog, AFGL-TR-83-0055
Richer H.B., 1971, ApJ 167, 521
Ridgway S.T., Carbon D.F., Hall D.N., 1978, ApJ 225, 138
Ridgway S.T., Keady J.J., 1988, ApJ 326, 843
Rouleau F., Martin P.G., 1991, ApJ 377, 526
Rowan-Robinson M., Harris S., 1983a, MNRAS 202, 767
Rowan-Robinson M., Harris S., 1983b, MNRAS 202, 797
Rowan-Robinson M., Lock T.D., Walker D.W., Harris S., 1986, MNRAS 222, 273

Sahai R., Wootten A., Clegg R.E.S., 1984, ApJ 284, 144
Sahai R., Liechti S., 1995, A&A 293, 198
Salpeter E.E., 1974, ApJ 193, 585
Salpeter E.E., 1977, ARA&A 15, 267
Schutte W.A., Tielens A.G.G.M., 1989, ApJ 343, 369
Simon T., 1976, AJ 81, 764
Sivagnanam P., Braz M.A., Le Squeren A.M., Tran Minh F., 1994, A&A 233, 112
Sopka R.J., et al., 1985, ApJ 294, 242
Strecker D.W., Ney, E.P., 1974, AJ 79, 797
te Lintel Hekkert P., Caswell J.L., Habing H.J., Hayes R.F., Norris R.P., 1990, A&AS 90, 327
te Lintel Hekkert P., Versteege-Hensel H.A., Habing H.J., Wiertz M., 1989, A&AS 78, 399
Vassiliadis E., Wood P.R., 1993, ApJ 413, 641
Walker A.R., 1979, SAAO 1, 112
Whitelock P.A., 1990, in: "Confrontation between stellar pulsation and evolution", ASP Conf. Ser. 11, eds. C. Cacciari and G. Clementini, p. 365
Whitelock P.A., Feast M.W., Marang F., Overbeek M.D., MNRAS, 1997, submitted
Whitelock P.A., Menzies J., Feast M.W., Marang F., Carter B., Roberts G., Catchpole R., Chapman J., 1994, MNRAS 267, 711
Winters J.M., 1994, Ph.D. thesis, Technische Universität Berlin
Winters J.M., Fleischer A.J., Gauger A., Sedlmayr E., 1994, A&A 290, 623
Winters J.-M., Fleischer A.J., Sedlmayr E., 1997, in: "Science with the VLT interferometer", Ed. TBD, p. TBD
Wood P.R., 1990, in: "From Miras to Planetary Nebulae", eds. M.O. Mennessier, A. Omont, Editions Frontieres, Gif-sur-Yvette, p. 67
Woolf T.G., 1973, ApJ 185, 229
Zuckerman B., Dyck H.M., 1986, ApJ 304, 394

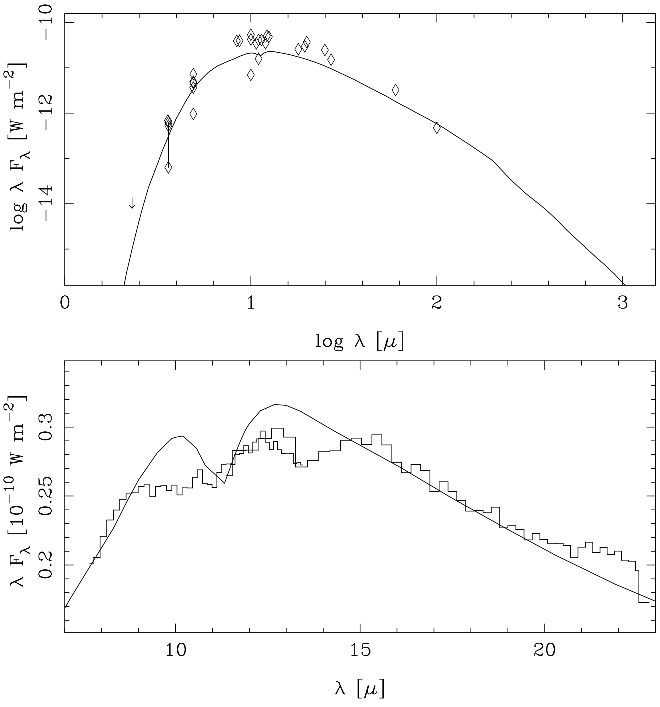

Figure 6. IRAS 01144+6658 (AFGL 190). The remaining part of this caption refers to Figs. 6-48 in general. The model is represented by the solid line, the observations by the symbols and the histogram, in case of the LRS spectra. The sub-mm data have error bars. Observations at minimum and maximum light are connected. Upper limits are indicated by a $\vee$. There usually is a kink in the model curve beyond 200 μm which is due to beam effects.

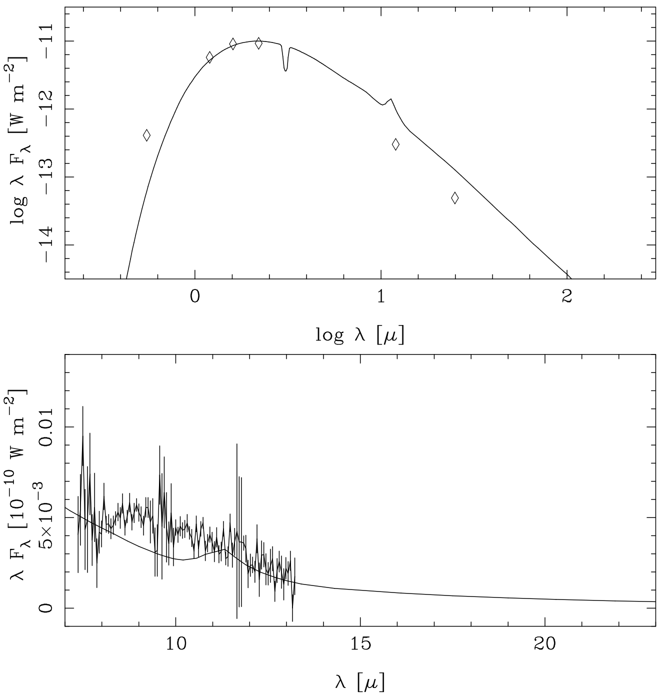

Figure 7. IRAS 02032+5636 (CN Per). The 8-13 μm spectrum represents the (unscaled) UKIRT spectrum.

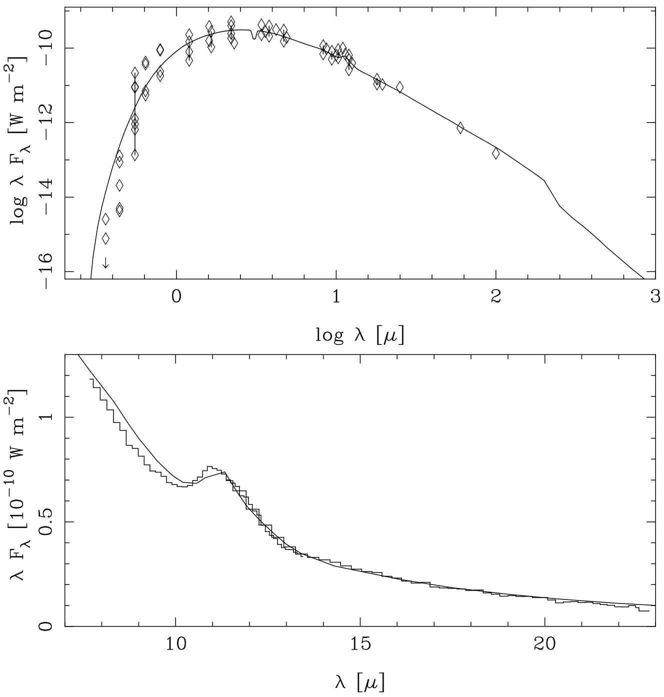

Figure 8. IRAS 02270−2619 (R For).

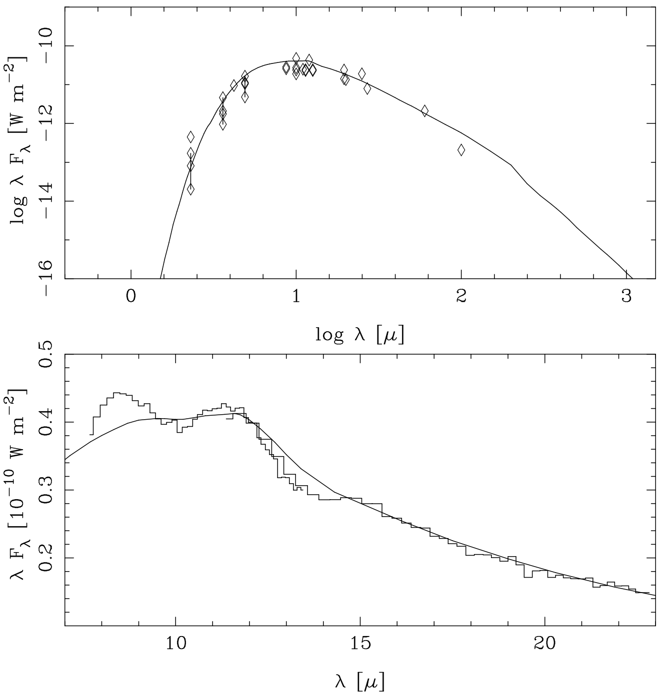

Figure 9. IRAS 02293+5749 (AFGL 341).

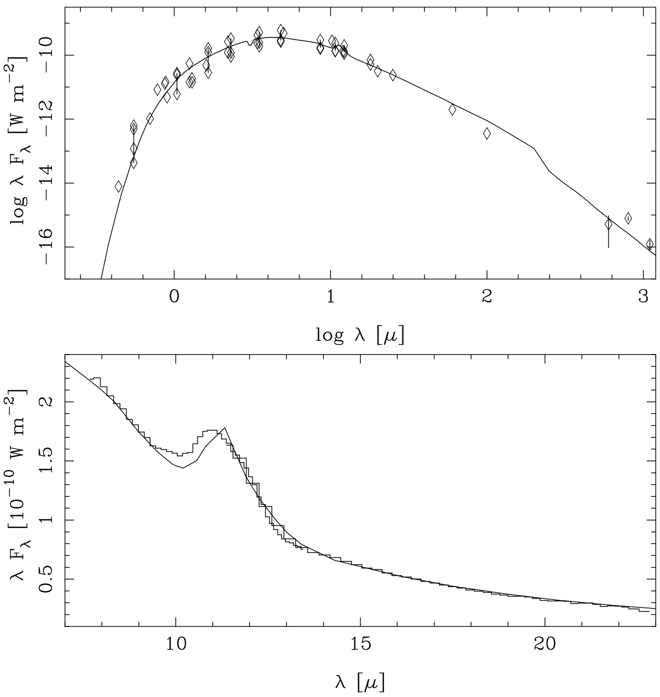

Figure 10. IRAS 03229+4721 (AFGL 489).

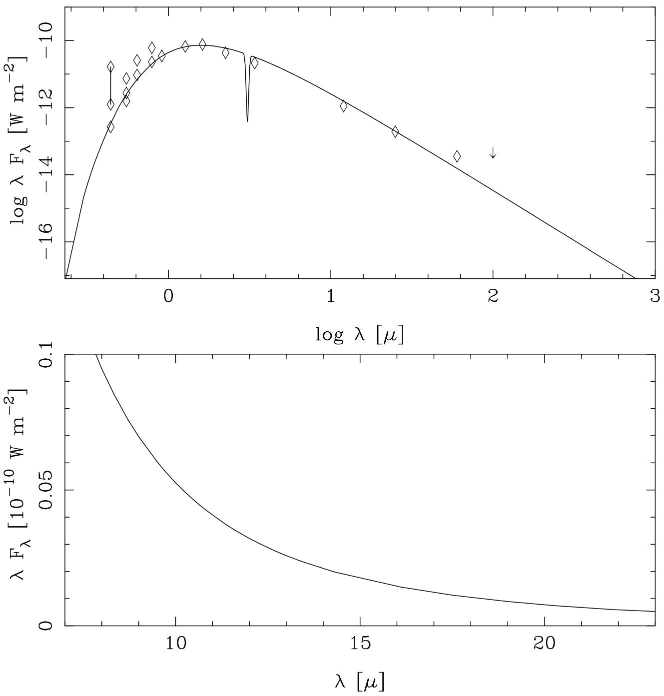

Figure 11. IRAS 03243+4400 (Y Per).

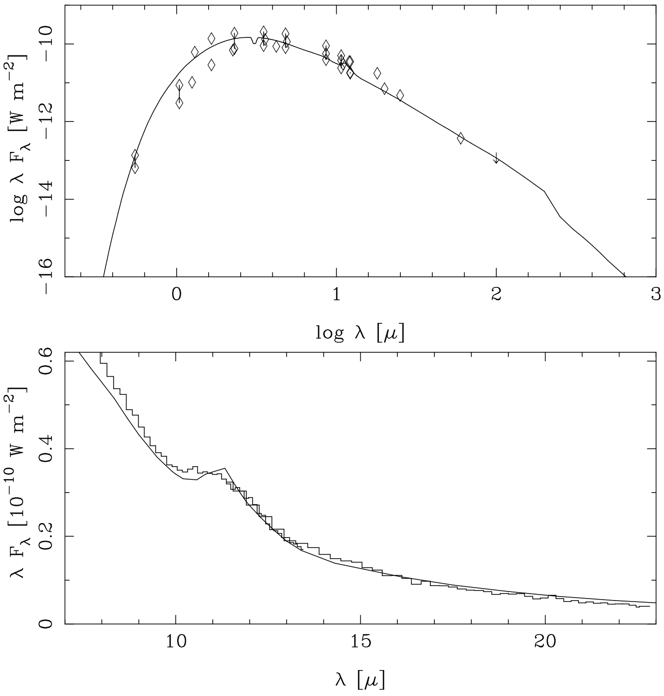

Figure 12. IRAS 03488+3943 (AFGL 527).

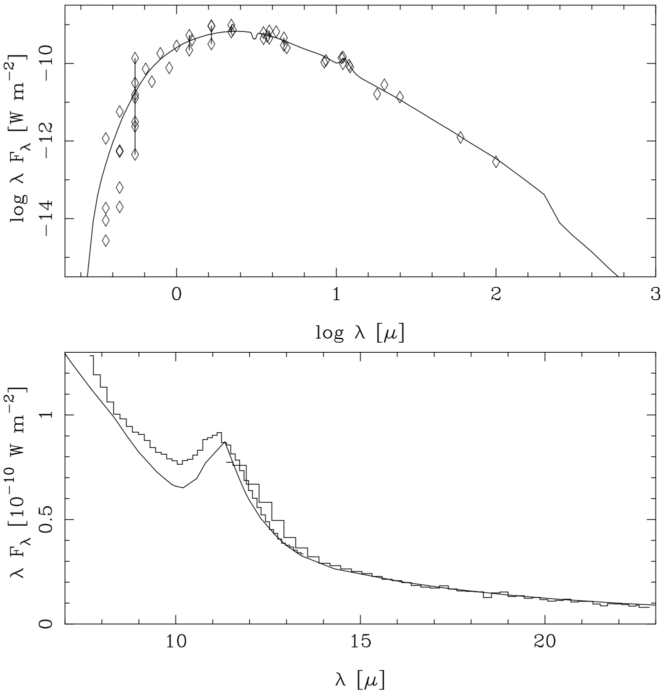

Figure 14. IRAS 04573−1452 (R Lep).

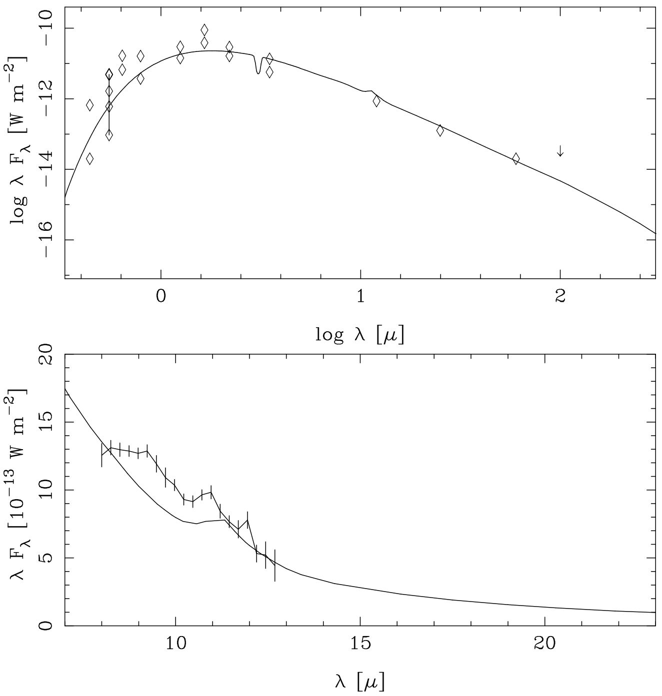

Figure 13. IRAS 04562+0803 (R Ori). The line with the error bars represents the AAT spectrum.

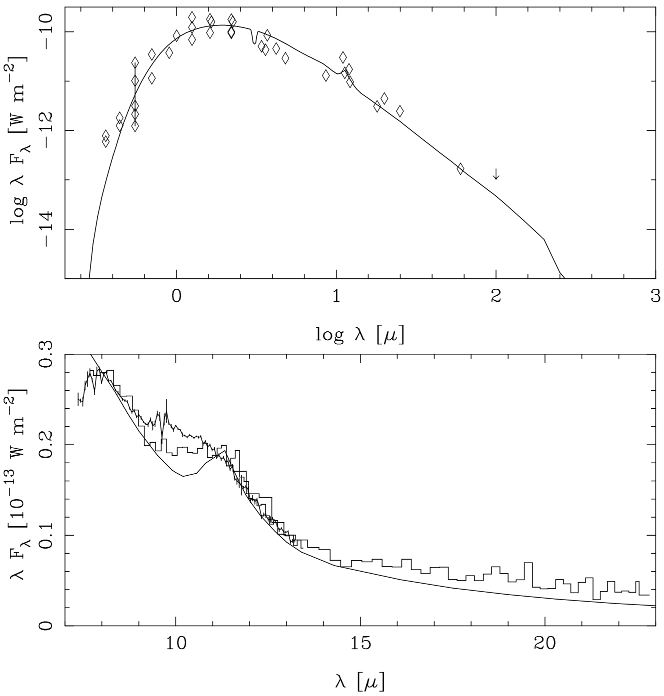

Figure 15. IRAS 05185+3227 (UV Aur). The 8-13 μm spectrum represents the UKIRT spectrum scaled by a factor of 1.8.

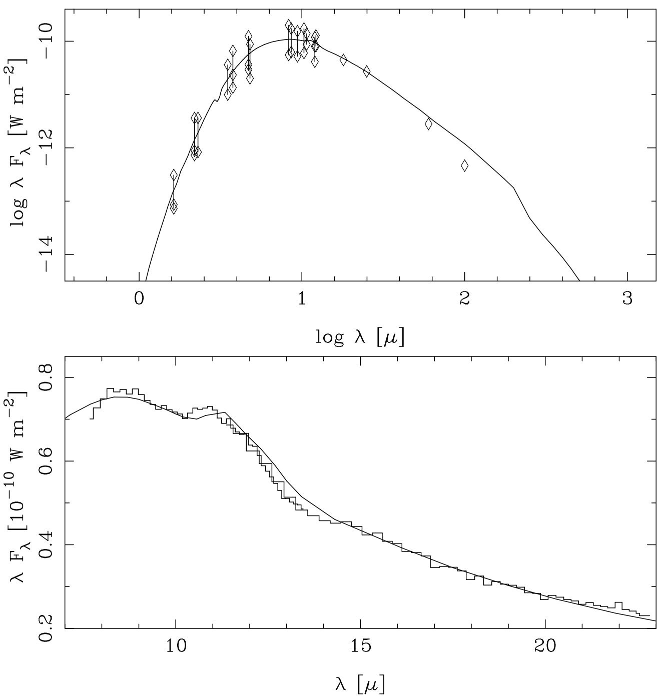

Figure 16. IRAS 06012+0328 (AFGL 865).

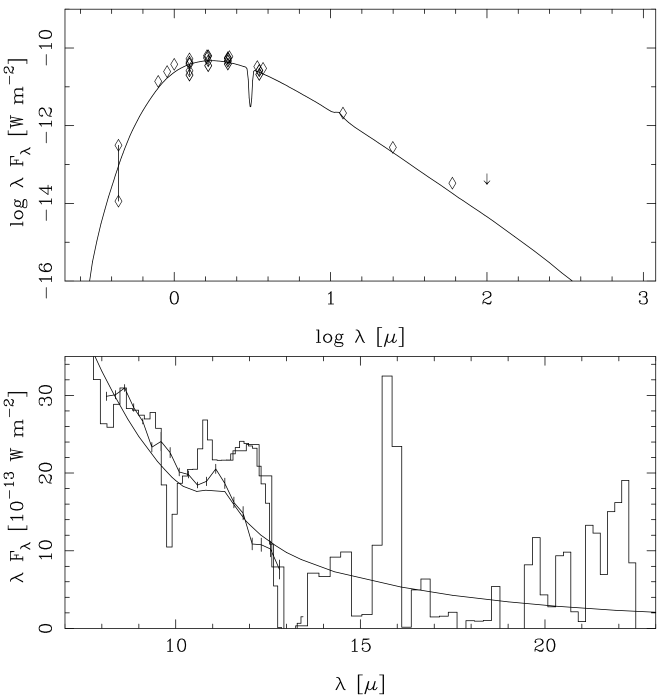

Figure 18. IRAS 06209+2503 (ZZ Gem). The 8-13 μm spectrum represents the (unscaled) AAT spectrum.

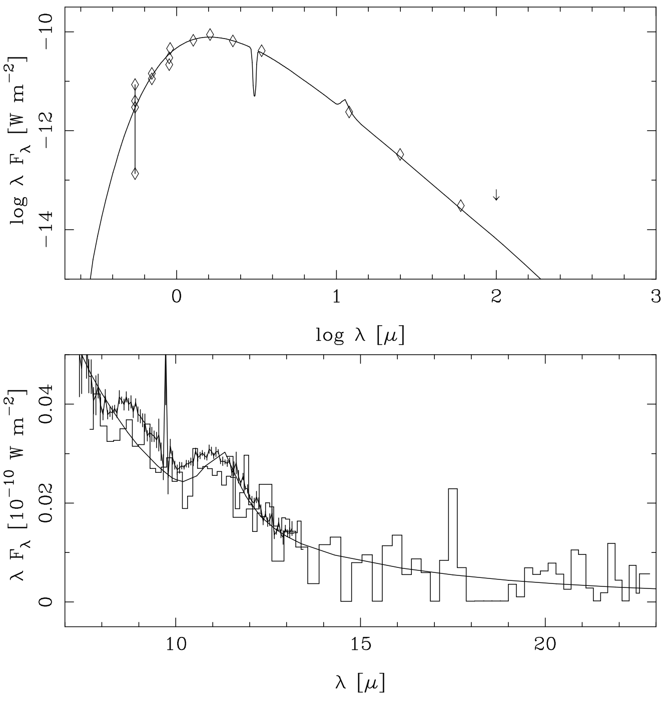

Figure 17. IRAS 06202+4743 (V Aur). The 8-13 μm spectrum represents the (unscaled) UKIRT spectrum.

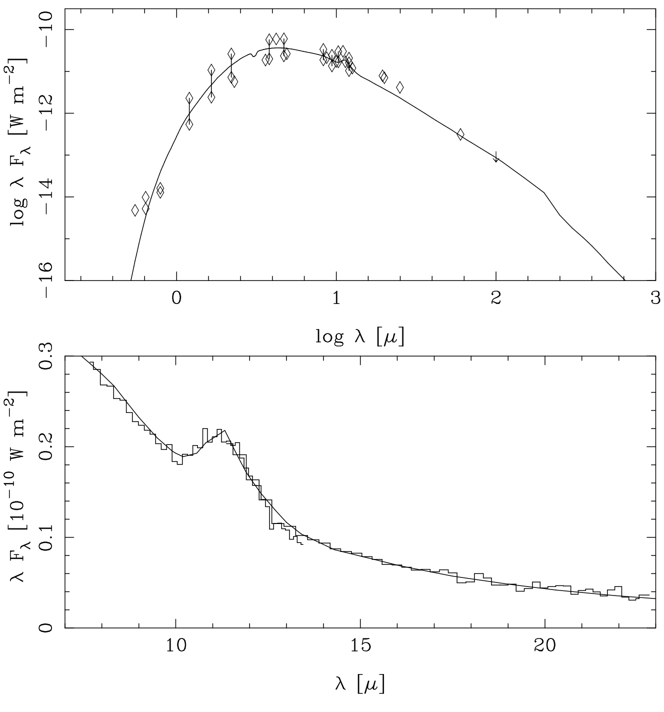

Figure 19. IRAS 06230−0930 (AFGL 935).

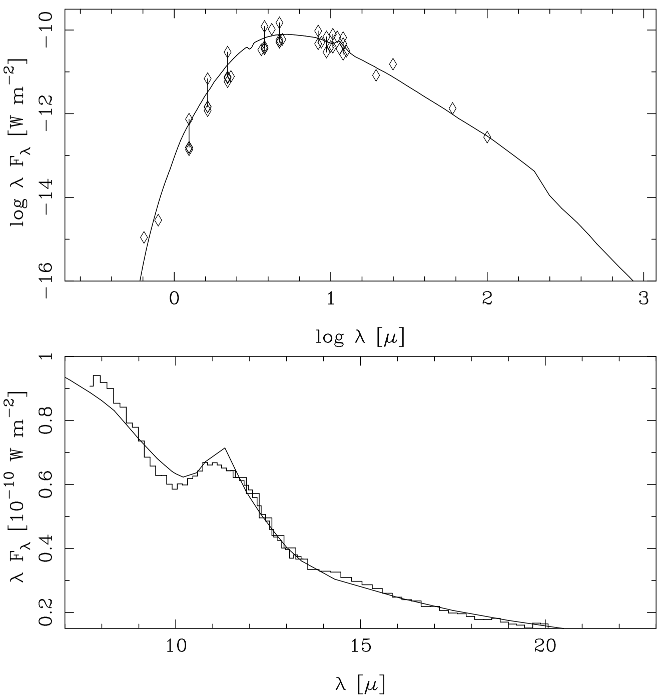

Figure 20. IRAS 06342−0328 (AFGL 971).

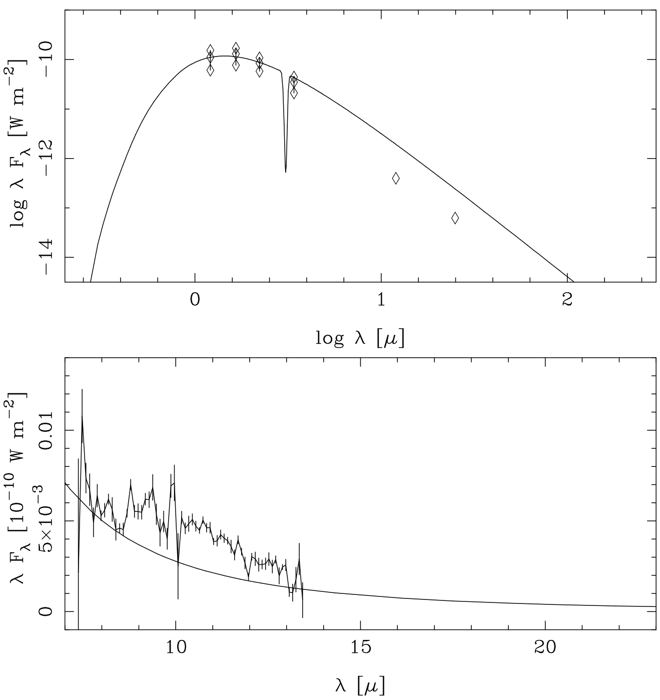

Figure 21. IRAS 06436+1840 (RT Gem). The 8-13 μm spectrum represents the (unscaled) UKIRT spectrum.

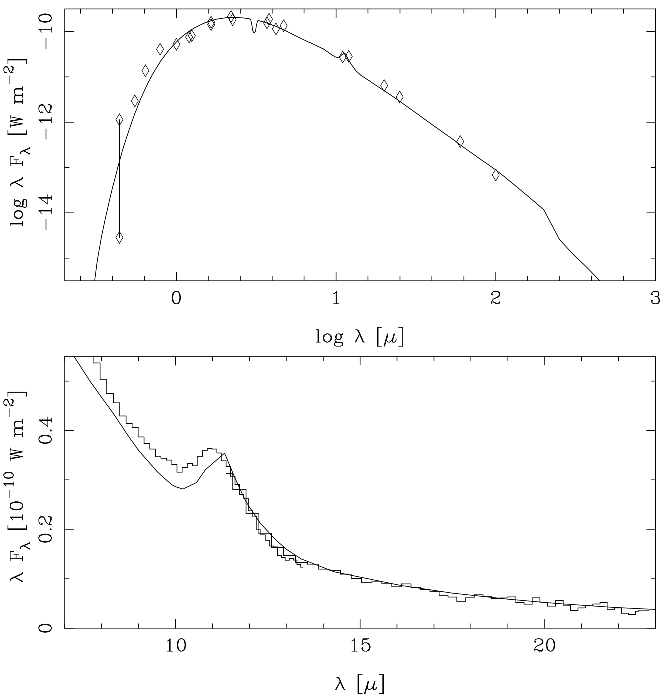

Figure 22. IRAS 06529+0626 (CL Mon).

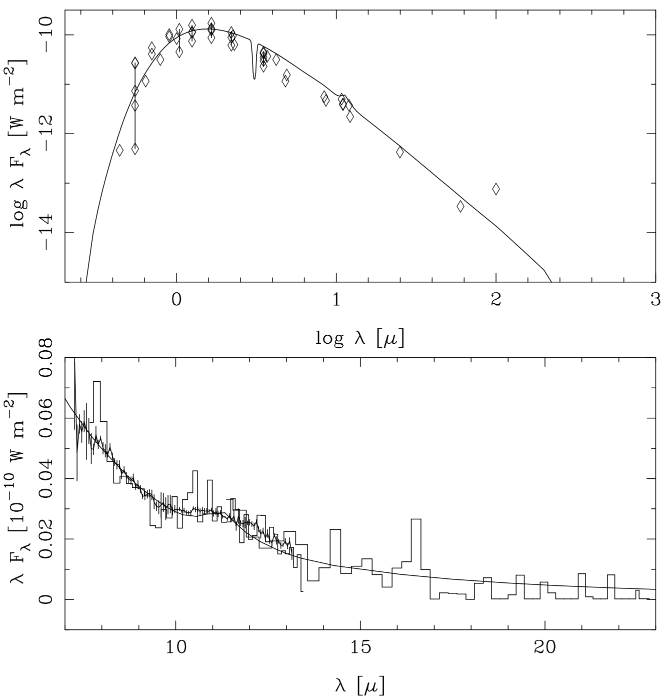

Figure 23. IRAS 07059+1006 (R CMi). The 8-13 μm spectrum represents the UKIRT spectrum scaled by a factor of 0.75.

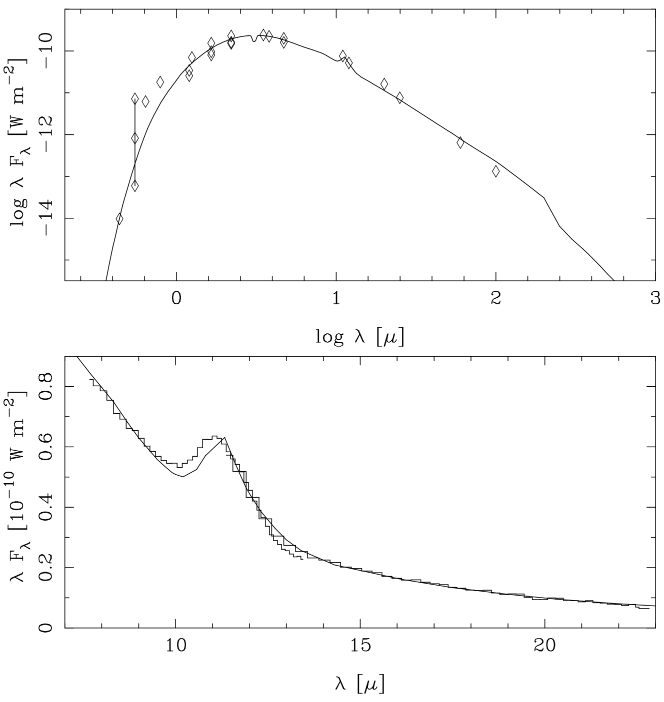

Figure 24. IRAS 07065−7256 (R Vol).

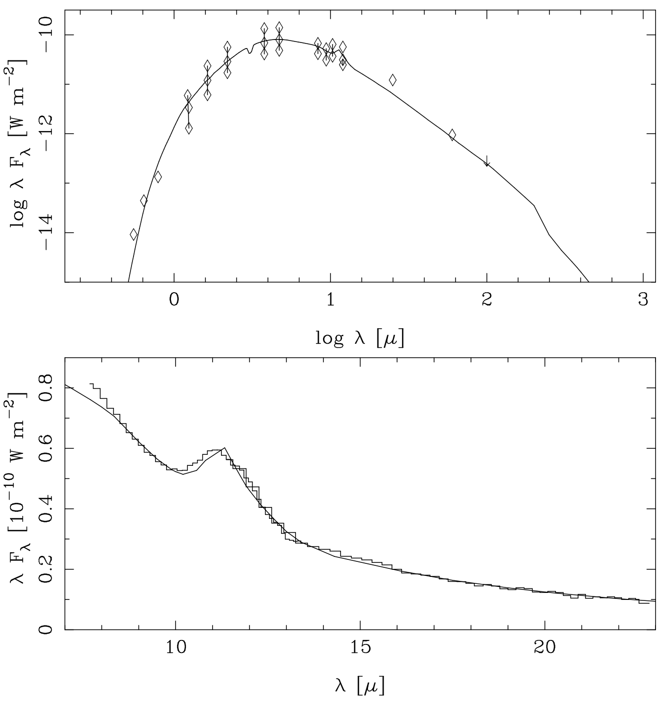

Figure 25. IRAS 07098−2012 (AFGL 1085)

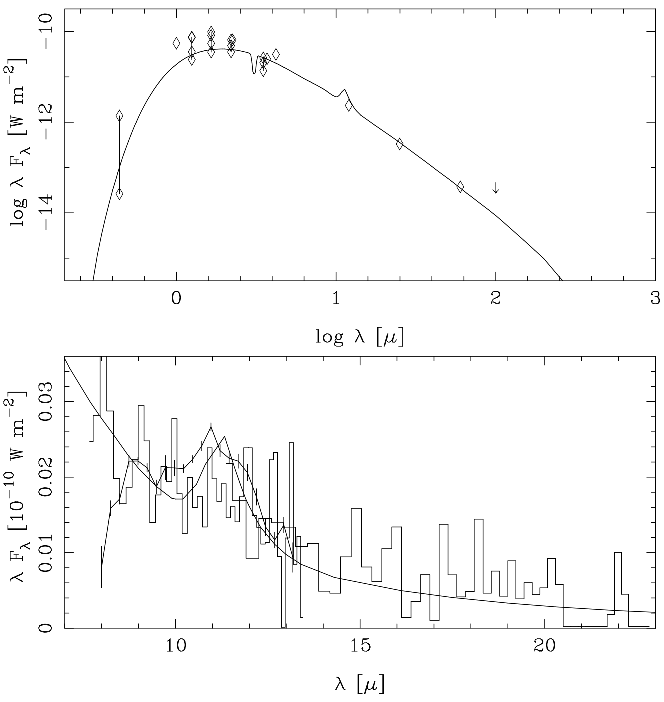

Figure 26. IRAS 07099+1441 (VX Gem). The 8-13 μm spectrum represents the AAT observations scaled by a factor of 1.5.

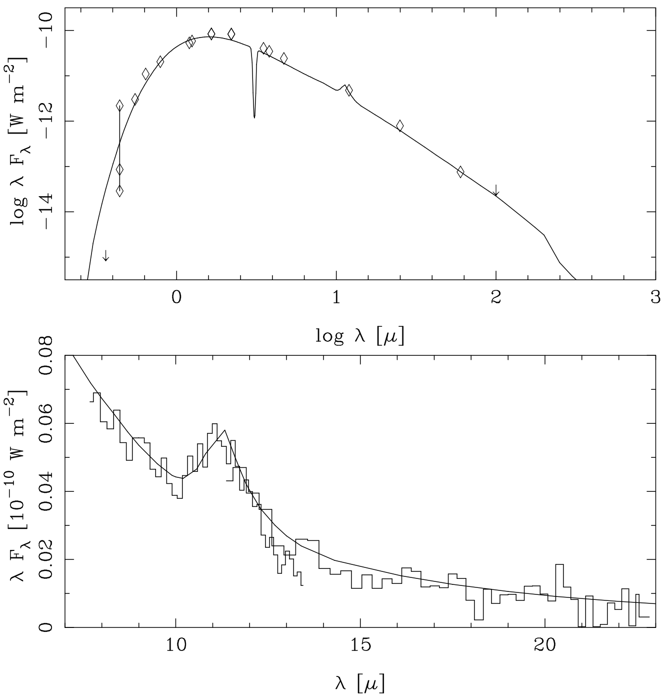

Figure 27. IRAS 08434−2801 (R Pyx)

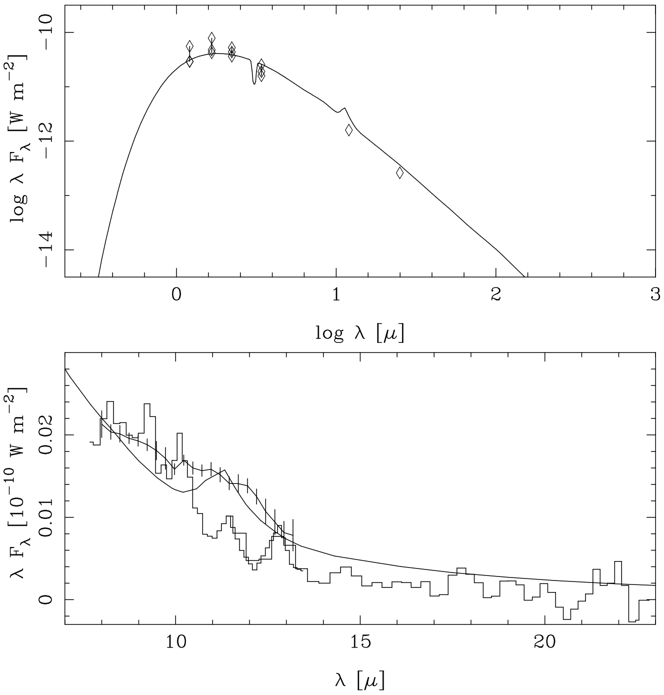

Figure 28. IRAS 10324−5358 (TV Vel). The 8-13 μm spectrum represents the AAT observations scaled by a factor of 0.66.

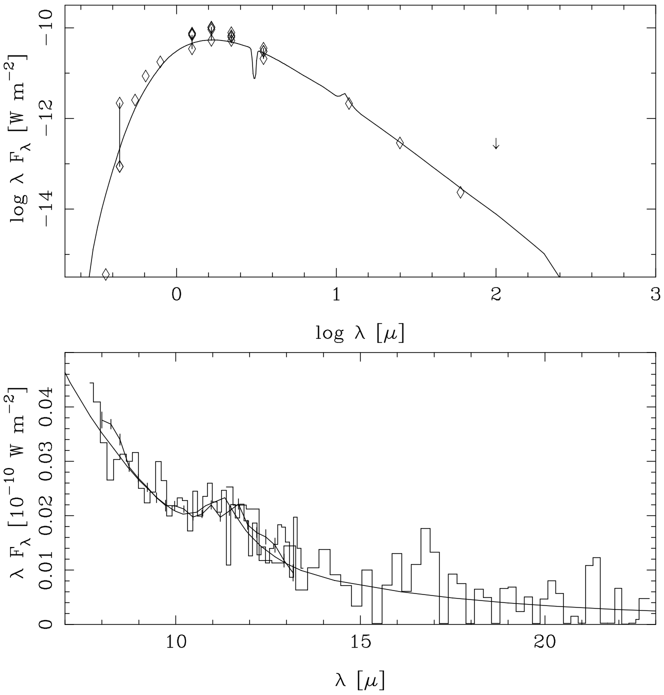

Figure 30. IRAS 12536−5737 (V Cru)

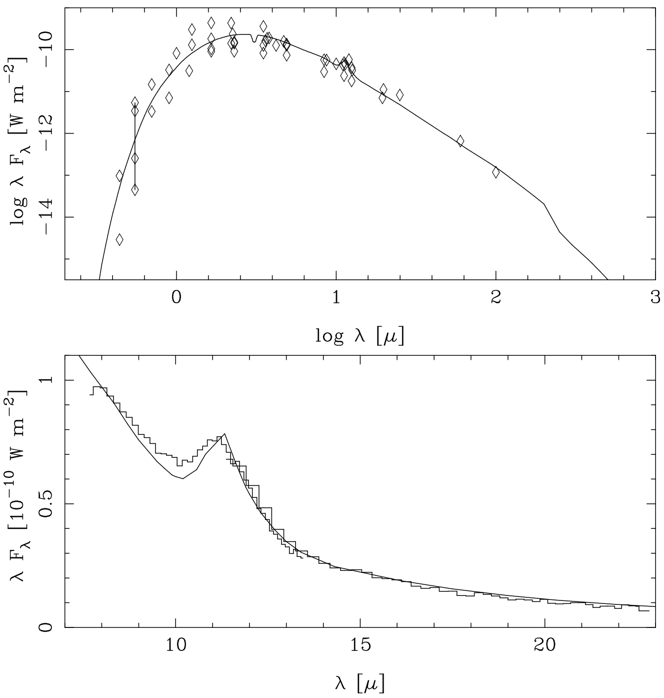

Figure 29. IRAS 12447+0425 (RU Vir)

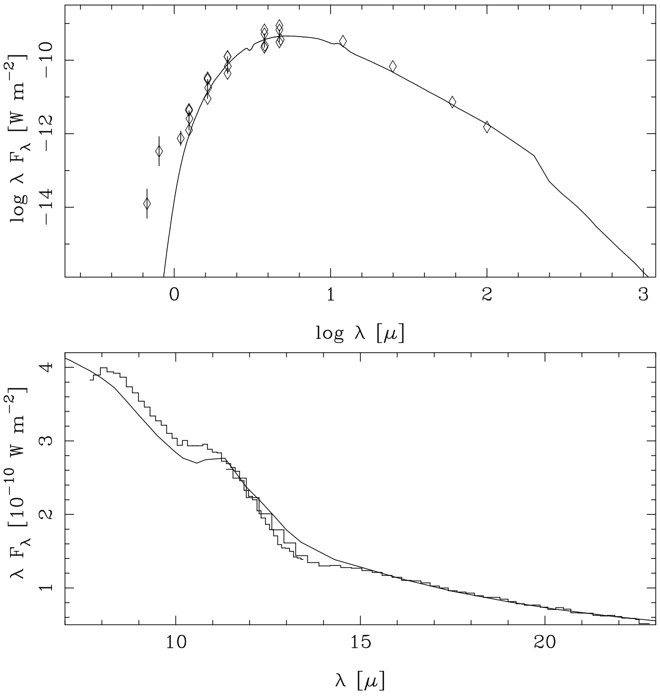

Figure 31. IRAS 15194−5115.

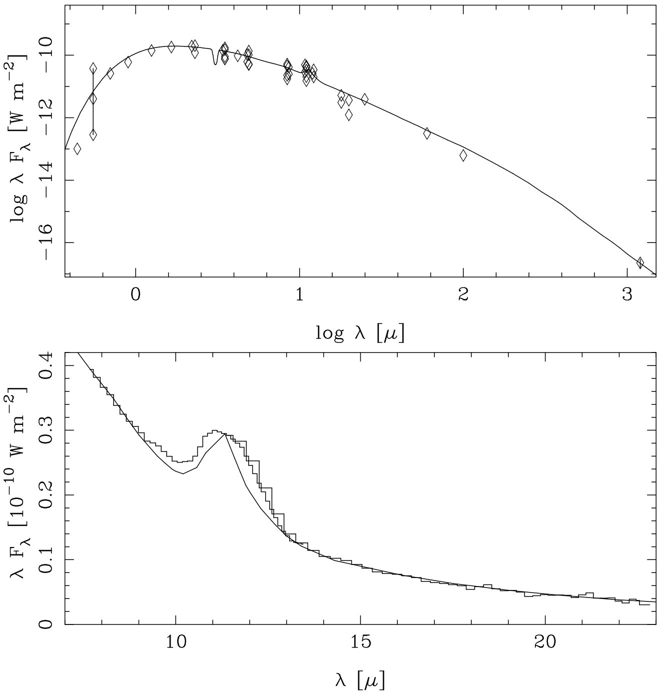

Figure 32. IRAS 15477+3943 (V CrB).

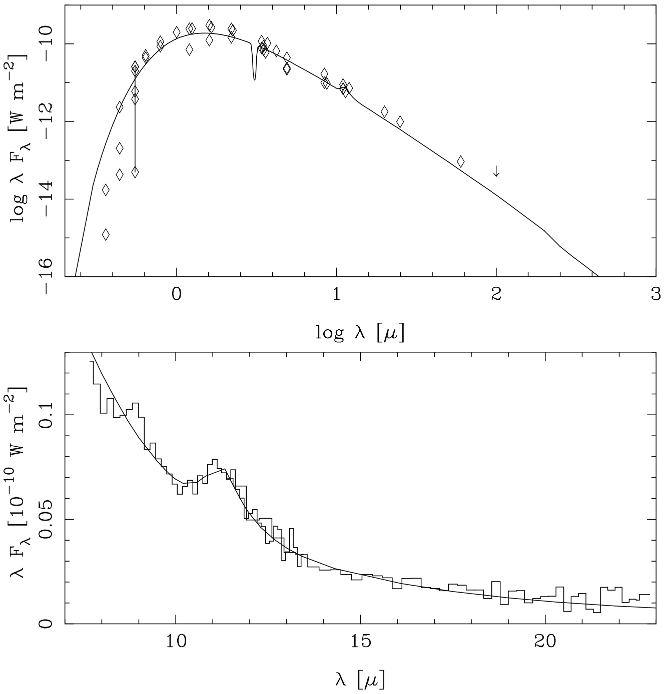

Figure 33. IRAS 16239−1218 (V Oph).

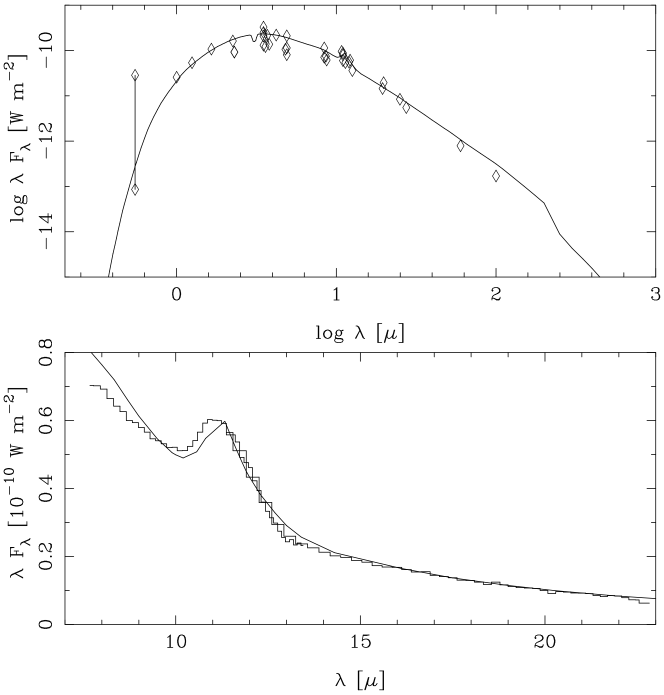

Figure 34. IRAS 17556+5813 (T Dra).

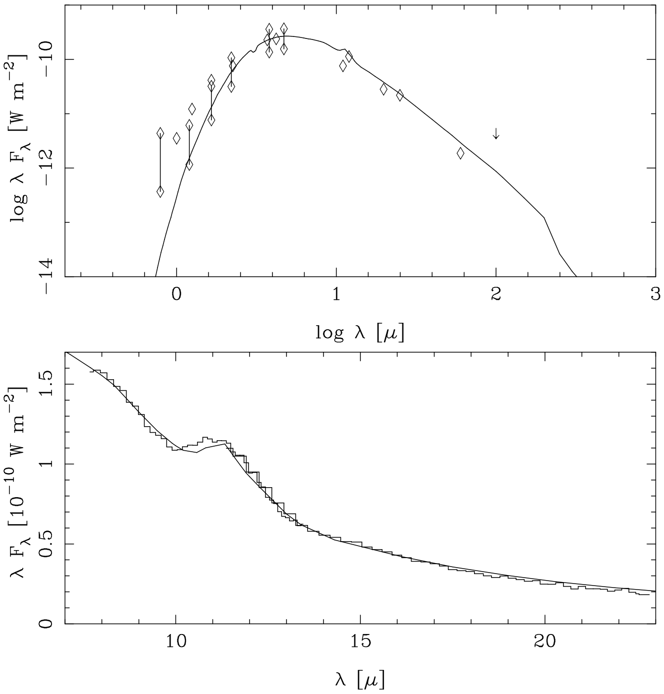

Figure 35. IRAS 19008+0726 (AFGL 2310).

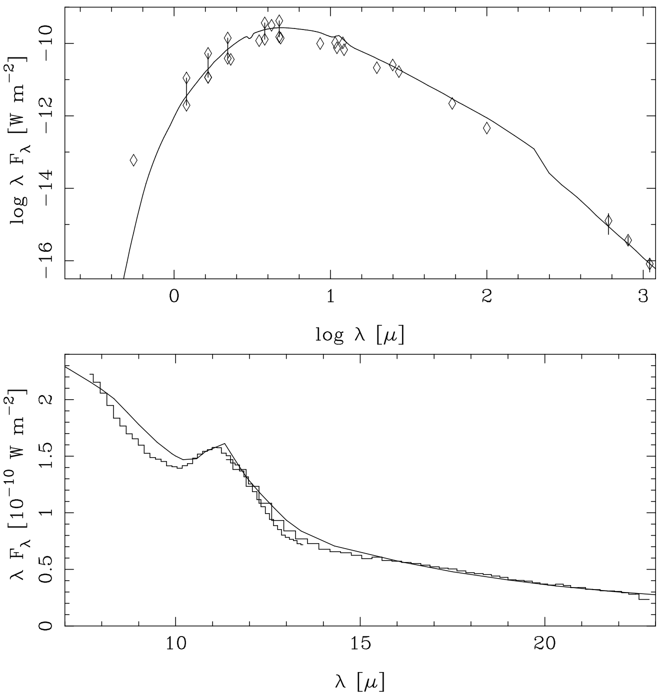

Figure 36. IRAS 19175−0807 (AFGL 2368).

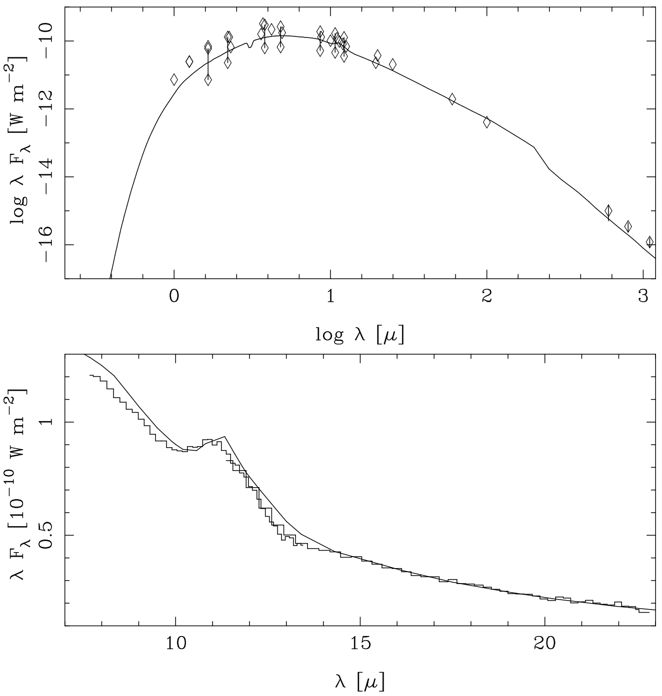

Figure 37. IRAS 19321+2757 (AFGL 2417).

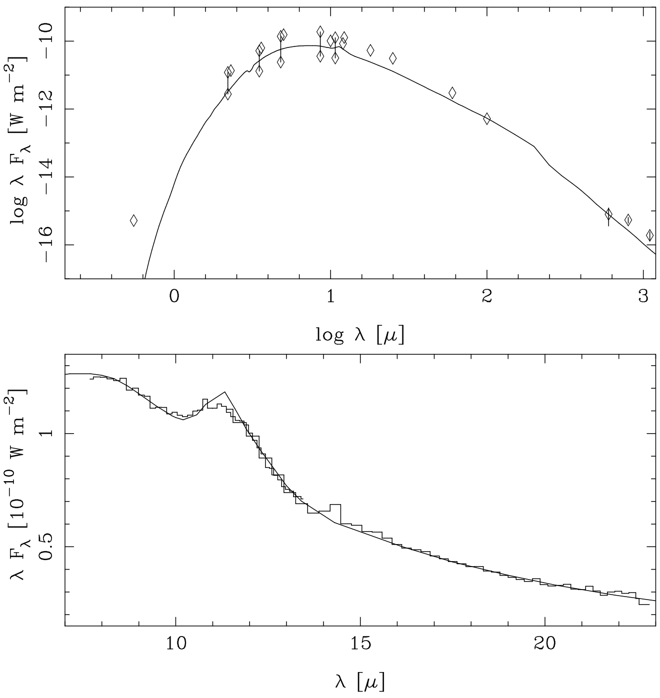

Figure 38. IRAS 19594+4047 (AFGL 2494).

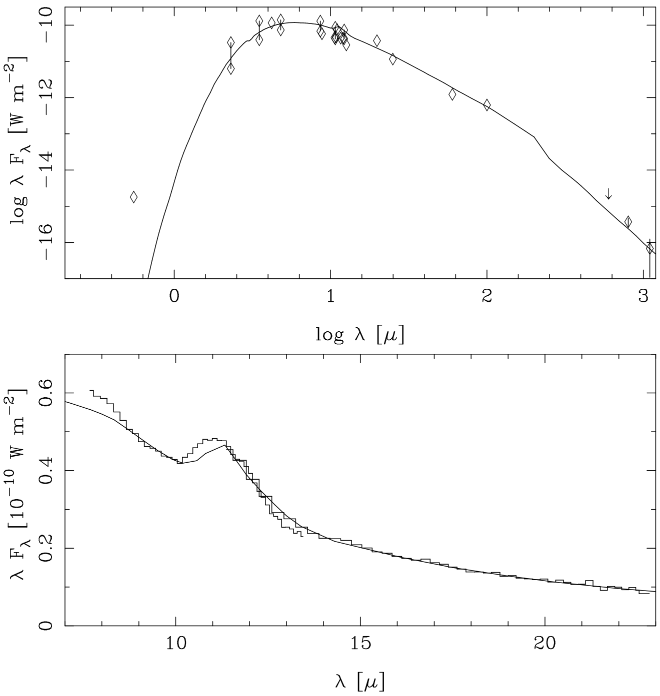

Figure 39. IRAS 20072+3116 (AFGL 2513).

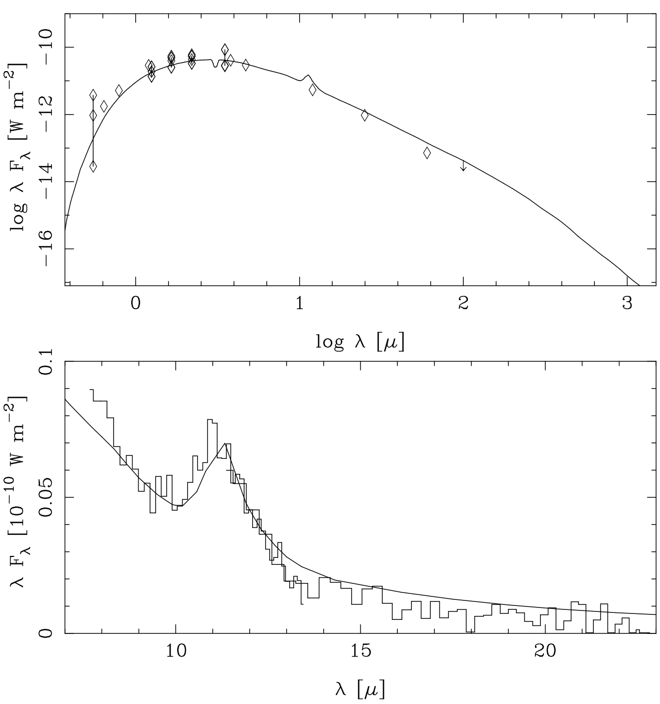

Figure 40. As Fig. 3 for IRAS 20085−1425 (R Cap).

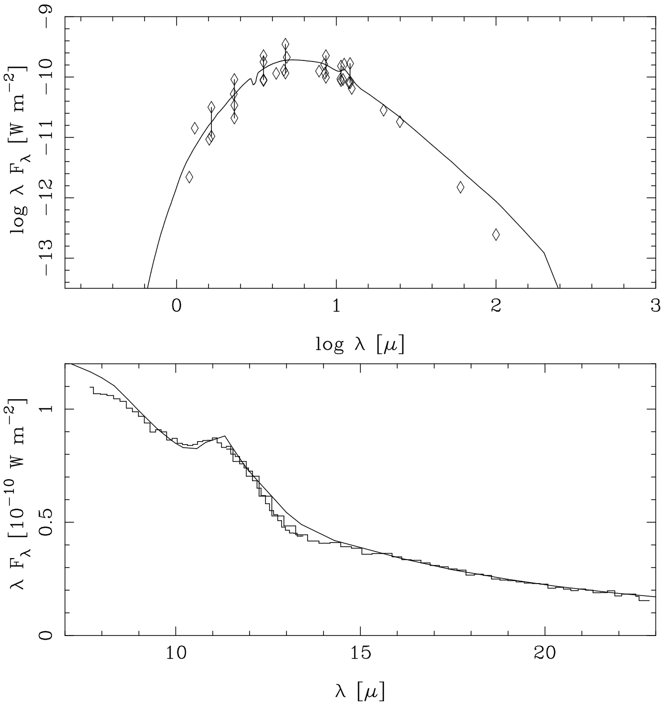

Figure 42. IRAS 20570+2714 (AFGL 2686).

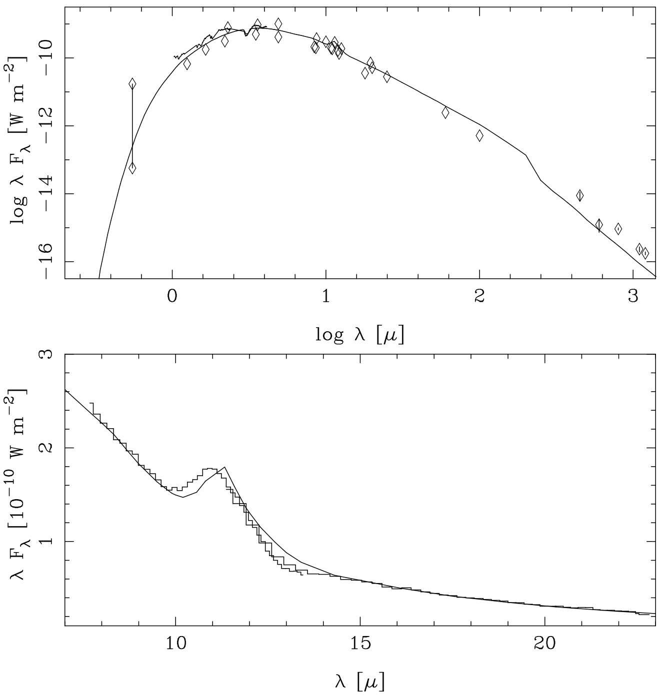

Figure 41. IRAS 20396+4757 (V Cyg).

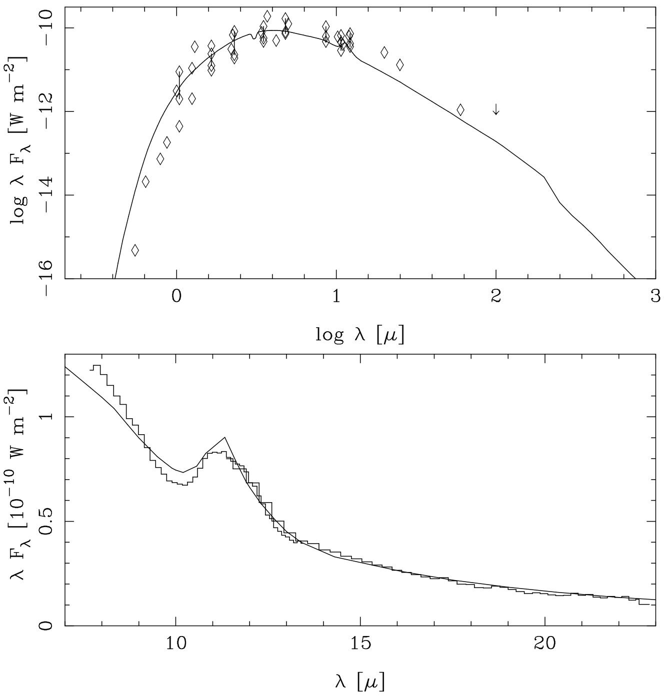

Figure 43. IRAS 21035+5136 (AFGL 2704).

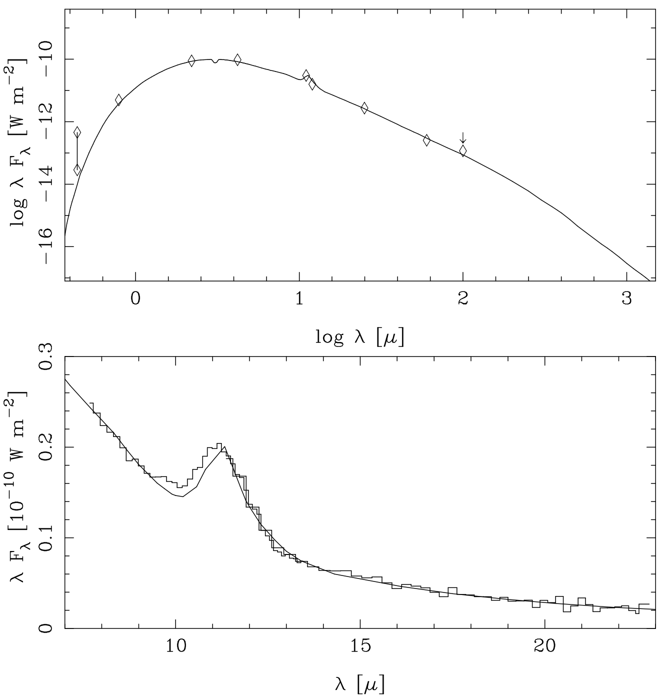

Figure 44. IRAS 21262+7000 (AX Cep).

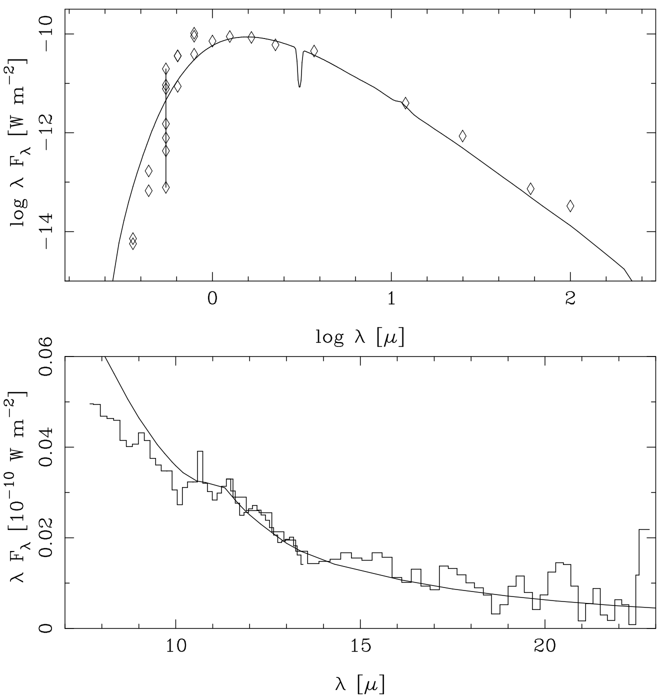

Figure 46. IRAS 22036+3315 (RZ Peg).

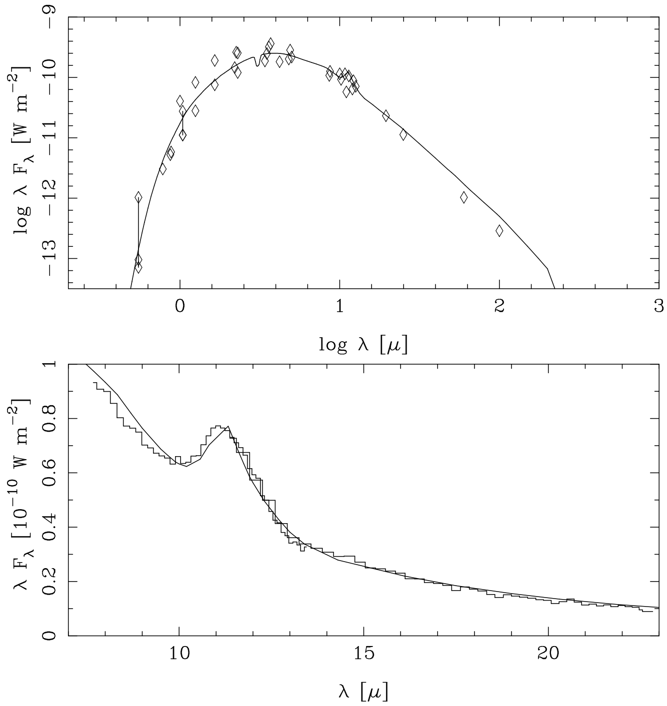

Figure 45. IRAS 21320+3850 (AFGL 2781).

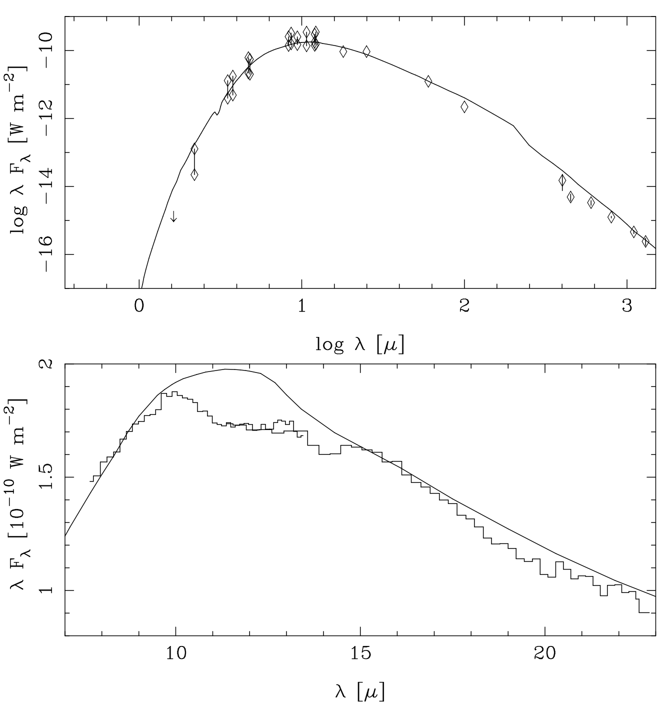

Figure 47. IRAS 23166+1655 (AFGL 3068).

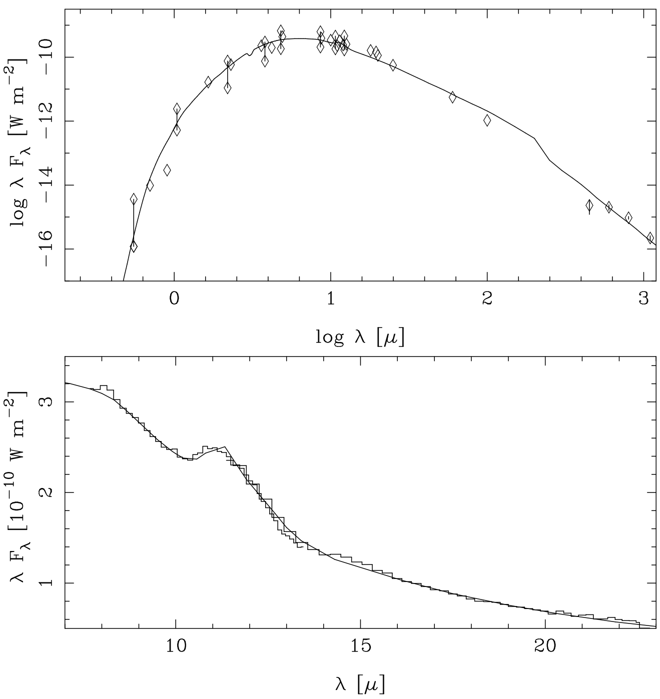

Figure 48. IRAS 23320+4316 (AFGL 3116).

APPENDIX A1: A SELF-CONSISTENT DETERMINATION OF MASS-LOSS RATE AND EXPANSION VELOCITY?

There has been much debate on the meaning and applicability of the formula $\dot{M} = \frac{L}{c\, v_\infty}$. It has been argued that the true mass-loss rate must be lower than that derived from this equation (see, e.g. Jura 1984, Zuckerman & Dyck 1986, Vassiliadis & Wood 1993). However, this is not the case (see Salpeter 1974, Gail & Sedlmayr 1986).

Recently, Netzer & Elitzur (1993) and Ivezić & Elitzur (1995) showed that $\dot{M}\ (v(r) - v(r_{\rm inner})) = \tau_{\rm F}(r)\ \frac{L}{c}$, or $\dot{M}\ v_\infty = \tau_{\rm F}\ \frac{L}{c}\ \left(1 - \frac{1}{\Gamma}\right)$ (when gravity is included) are the correct formula, where Γ is the ratio of the radiative to gravitational force.

In these equations, the gas velocity is usually assumed to be known, e.g. taken from CO and/or OH observations. In other words, if Γ were known and the flux-weighted optical depth derived from radiative transfer modelling, the mass loss rate can be calculated.

As shown below, the value of Γ can be written down exactly but is then in a form not suitable for practical application. A second point discussed below is that the same basic force equation can be solved to give the velocity structure. Since the terminal velocity of the wind is known from observations this in principle gives a contraint on the radial dependence of the opacity in the wind.

The momentum equation for the gas, assuming that the outward force is radiation pressure, is:

$$\rho v \frac{dv}{dr} = \frac{\kappa_F L}{4\pi r^2 c} - \frac{\rho G M_\star}{r^2}, \tag{A1}$$

where κ_F is the flux-averaged absorption coefficient at radius r. With mass conservation, this can be re-written as

$$\dot{M}\frac{dv}{dr} = \frac{L}{c}\kappa_F - 4\pi G M_\star \rho. \tag{A2}$$

The only quantities that depend on r are v, κ_F, and ρ, all other are constant. Integration gives

$$\dot{M}(v - v_0) = \frac{L}{c}\tau_F(r) - 4\pi G M_\star \int_{r_0}^{r} \rho\, dr, \tag{A3}$$

where r_0 and v_0 are the radius and velocity at the inner boundary and $\tau_F(r) = \int_{r_0}^{r} \kappa_F(r) dr$. Taking the $r \to \infty$ limit gives

$$\dot{M}(v_\infty - v_0) = \tau_F \frac{L}{c}\left(1 - \frac{1}{\Gamma^{(1)}}\right), \tag{A4}$$

where $\tau_F = \tau_F(r \to \infty)$ and

$$\Gamma^{(1)} = \frac{L}{4\pi c G M_\star} \frac{\int_{r_0}^{\infty} \kappa_F(r)\, dr}{\int_{r_0}^{\infty} \rho\, dr}. \tag{A5}$$

This relation is exact.

Alternatively, equation (A1) can be re-written as

$$v\frac{dv}{dr} = \frac{\chi_F L}{4\pi r^2 c} - \frac{G M_\star}{r^2}, \tag{A6}$$

where χ_F is the flux-average of $\chi_\nu = \kappa_\nu/\rho$, the absorption coefficient per unit mass. This gives

$$\frac{dv^2}{dr} = \frac{2 G M_\star}{r^2}\left(\Gamma^{(2)} - 1\right), \tag{A7}$$

where

$$\Gamma^{(2)} = \frac{L}{4\pi c G M_\star} \frac{\kappa_F(r)}{\rho(r)}. \tag{A8}$$

$\Gamma^{(2)}$ can be re-written using the definition of $\kappa_F = \pi\, a^2\, Q_{\rm F}\, n_{\rm d}(r)$ and the continuity equation for the dust ($\dot{M}_{\rm d} = 4\ \pi\ r^2\ n_{\rm d}(r)\ m_{\rm d}\ v_{\rm d}(r)$) and the gas ($\dot{M} = 4\pi\, r^2\, \rho\, v(r)$) as:

$$\Gamma = \frac{3\ Q_{\rm F}\ L\ \Psi\ v(r)}{16\ \pi\ a\ \rho_{\rm d}\ c\ G\ M_\star\ v_{\rm d}(r)}. \tag{A9}$$

where $n_{\rm d}(r)$ is the dust particle number density and $m_{\rm d} = \frac{4}{3}\ \pi\ a^3\ \rho_{\rm d}$, the mass of a single dust particle.

Equation (A7) can be solved to give

$$v^2 - v_0^2 = \frac{L}{2\pi c}\int_{r_0}^{r} \frac{\chi_F dr}{r^2} - 2 G M_\star \left(\frac{1}{r_0} - \frac{1}{r}\right), \tag{A10}$$

again, an exact result within the model assumptions.

From Eq. (A10), the velocity at infinity can be written as

$$v_\infty^2 - v_0^2 = \frac{2 G M_\star}{r_0}\left(\Gamma^{(3)} - 1\right), \tag{A11}$$

where

$$\Gamma^{(3)} = \frac{L}{4\pi c G M_\star}\int_{r_0}^{\infty} r_0 \frac{\chi_F(r)}{r^2} dr. \tag{A12}$$

Equations (A1) and (A6) are completely equivalent and so are their solutions (A3) and (A10). In other words back-substituting the velocity solution $v(r)$ from Eq. (A10) in Eq. (A3) should give an identity.

Direct application of Eq. (A4) to derive the mass-loss rate is hindered by the fact that Γ depends on integral quantities that are unknown. Below an approximation is introduced to circumvent this. It is explicitly verified that with this approximation the self-consistency between Eq. (A4) and (A11) is not violated.

Assuming that $\Gamma^{(2)}$ (or simply Γ hereafter) is independent of radial distance, Eq. (A7) can be integrated, using $v = v_0$ at $r = r_0$ as a boundary condition (see e.g. Habing et al. 1994):

$$v^2(r) = v_0^2 + 2\,G\,M_\star\,(\Gamma - 1)\,\left(\frac{1}{r_0} - \frac{1}{r}\right); \tag{A13}$$

from which follows that the terminal gas velocity is:

$$v_{\rm theory} = \sqrt{v_0^2 \,+\, \frac{2\,G\,M_\star}{r_0}\,(\Gamma - 1)}. \tag{A14}$$

Next the dust velocity law needs to be derived. Its radial dependence should be very similar to Eq. (A13) to fulfil the requirement that Γ is independent of radius, as we will replace $Q_{\rm F}(r)$ by $Q_{\rm F}(\infty)$. However, we need to manipulate Eq. (A13) to arrive at a equation that can be integrated analytically. As v_0 should only be important close to r_0, Eq. (A13) is written in the form

$$v_{\rm d}^2(r) = v_0^2\,\left[\frac{r_0}{r}\right] + (v_{\rm theory}^2 - v_0^2)\,\left(1 - \frac{r_0}{r}\right), \tag{A15}$$

where the “fudge-factor” (r_0/r) gives the exact formula for $r = r_0$. Rearranging terms, the shape of the dust velocity law can be written as (also see Habing et al. 1994):

$$v_{\rm d}(r) = v_{\rm d}(\infty)\,\sqrt{\frac{x - y_0}{x}}, \tag{A16}$$

with $x = r/r_0$, and y_0 defined as

$$y_0 = 1 - \frac{v_0^2}{v_\infty^2 - v_0^2}. \tag{A17}$$

The continuity equation of the dust specifies that

$$\dot{M}_{\rm d} = 4\,\pi\,r^2\,v_{\rm d}(r)\,n_{\rm d}(r)\,m_{\rm d}. \tag{A18}$$

Combined with the definition of the optical depth

$$\tau_\lambda = \int_{r_0}^{\infty} \pi\,a^2\,Q_\lambda\,n_{\rm d}(r)\,dr, \tag{A19}$$

it follows that:

$$\tau_\lambda = \frac{(3Q_\lambda/4\,a\,\rho_{\rm d})\,\dot{M}_{\rm d}}{4\,\pi\,v_{\rm d}(\infty)\,r_0}\,\int_1^\infty \frac{1}{\sqrt{(x - y_0)/x}}\,\frac{1}{x^2}\,dx. \tag{A20}$$

The integral can be evaluated analytically, and the result is $Y \equiv \frac{2}{y_0}\,(1 - \sqrt{1 - y_0})$.

Now we are ready to proceed.

By construction the radial dependence of the gas and dust velocity are essentially equal, and $\frac{v(r)}{v_{\rm d}(r)}$ is replaced by $\frac{v(\infty)}{v_{\rm d}(\infty)}$. Using the definition of the dust-to-gas ratio ($\Psi = \dot{M}_{\rm d}/\dot{M}$), Γ can be written as:

$$\Gamma = \frac{(3Q_{\rm F}(\infty)/4\,a\,\rho_{\rm d})\,L\,v_\infty}{4\,\pi\,c\,G\,M_\star\,v_{\rm d}(\infty)}\,\frac{\dot{M}_{\rm d}}{\dot{M}} \tag{A21}$$

For the dust mass-loss rate, we invert Eq. (A19) and substitute it in Eq. (A21):

$$\Gamma = \frac{Q_{\rm F}\,\tau_\lambda\,L\,r_0\,v_\infty}{Q_\lambda\,c\,G\,M_\star\,Y}\,\frac{1}{\dot{M}}. \tag{A22}$$

For the mass-loss rate, we now substitute Eq. (A4), with $\Gamma^{(1)}$ replaced by Γ:

$$\dot{M} = \tau_{\rm F}\,\frac{L/c}{v_\infty - v_0}\,\left(1 - \frac{1}{\Gamma}\right). \tag{A23}$$

This results in:

$$\Gamma - 1 = \left(\frac{Q_{\rm F}\,\tau_\lambda}{Q_\lambda\,\tau_{\rm F}}\right)\,\frac{r_0\,v_\infty\,(v_\infty - v_0)}{G\,M_\star\,Y}. \tag{A24}$$

The first term between parenthesis is identical to unity, because $\tau_\lambda \sim Q_\lambda$, and similarly for the flux-weighted quantity. Substituting the expression for Γ into Eq. (A14), gives

$$v_{\rm theory} = \sqrt{v_0^2 \,+\, v_\infty\,(v_\infty - v_0)\,y_0/(1 - \sqrt{1 - y_0})}. \tag{A25}$$

One can make an expansion in (v_0/v_∞) and show that:

$$v_{\rm theory} = v_\infty\,\sqrt{1 + \frac{1}{2}\,(v_0/v_\infty)^3 + O((v_0/v_\infty)^4)}. \tag{A26}$$

This shows that for the given approximations for Γ, Eq. (A14) and Eq. (A24) are self-consistent to a very high degree.

As the model fits were made taking a constant velocity while the approach to calculate the mass loss rate requires a certain dust velocity law, a correction to the originally derived dust mass loss rates must be made. As the fits to the SEDs exclusively depend on the optical depth this implies that the dust mass loss rates listed in Tab. 3 have to be divided by Y, following Eq. (A20).

APPENDIX A2: SELECTION OF A SAMPLE OF O-RICH MIRAS AND OH/IR STARS

To compare some observational properties of Carbon stars and O-rich stars, a sample of O-rich Miras and OH/IR stars is constructed. The primary interest is in period, NIR photometry on the ESO system and expansion velocity.

For practical purposes the data gathering was done in two steps, that regarding optical Miras and that concerning OH/IR stars. One of us (FK) selected from the 4th edition of the GCVS all O-rich confirmed Miras with confirmed periods with an IRAS FQUAL = 3 detection at 12 and 25 μm. This amounts to 1138 stars. For 133 of these $JHKL'M$ photometry is available on the ESO system. The photometry is taken from a database of one of the authors (FK). For 32 stars the expansion velocity based on CO data is available from Loup et al. (1993), and for another 16 from Groenewegen et al. (1996b). To have a larger sample of expansion velocities, OH data was considered. This search was helped by the information provided by Drs. J. Lepine and R. Ortiz who provided their database on OH/IR stars (private communication; Lepine et al. 1995, Ortiz & Maciel 1996). This provided expansion velocities for 83 O-rich Miras, 64 of which have no CO velocity. When both are available, the CO velocity is preferred. The OH velocity is multiplied by a factor of 1.12, for reasons discussed below.

Regarding the OH/IR stars, the first step was to search the literature for pulsation periods. This search was also helped by the information provided by Drs. Lepine and Ortiz, but done independently. Periods were taken from Engels et al. (1981), Engels et al. (1983), Lockwood (1985), Jones et al. (1990), Le Bertre (1993), Whitelock et al. (1994), Gaylard & West (1995), Chapman et al. (1995), Jiminez-Esteban et al. (1997), Joyce et al. (1997). Searches specifically aimed at finding OH/IR stars in the galactic bulge are excluded, as the associated photometry may be more susceptible to interstellar extinction than the presumably local sample selected now.

Stars already in the GCVS sample were excluded. Ninety-two stars remain. NIR photometry on the ESO system was compiled for 70 stars (Fouque et al. 1992, Guglielmo et al. 1993, Le Bertre 1993, Engels et al. 1981, 1983, Nyman et al. 1993a), as well as CO velocities for 35 stars (Loup et al. 1993) and OH velocities for 67 stars (te Lintel Hekkert 1989, 1990, Le Squeren et al. 1992, Sivagnanam et al. 1994), when available. Note that in some cases the OH profiles show only one peak, in which case no OH expansion velocity is available.

It is common to derive the CO expansion velocities from half the width at zero intensity, while it is common to derive the OH expansion velocity as half the width between the two peaks. The latter underestimates the true terminal velocity. From 22 stars with both CO and OH velocity, the geometric mean value of $v(\mathrm{CO})/v(\mathrm{OH})$ is 1.12. The CO velocity is preferred over the OH velocity. When no CO velocity is available, the OH velocity multiplied by 1.12 is used.